NAG 5-629

THE STRUCTURE OF GALACTIC HI IN DIRECTIONS OF LOW TOTAL COLUMN DENSITY

Felix J. Lockman

National Radio Astronomy Observatory*

Charlottesville, Virginia

and

Keith Jahoda and Dan McCammon

Physics Department, University of Wisconsin

Madison, Wisconsin

*The National Radio Astronomy Observatory is operated by Associated Universities, Inc., under contract with the National Science Foundation.

ABSTRACT

We have made a detailed 21 cm study of areas that have the smallest known amount of HI in the northern sky. These observations were corrected for stray radiation using a method described in an Appendix, and have an estimated uncertainty in N_{HI} of $\leq 5 \times 10^{18}$ cm^{-2}. The region of main interest, around $\alpha = 10^h45^m$, $\delta = 57°20'$, has a minimum N_{HI} of 4.5×10^{19} cm^{-2}. Spectra taken at 21' resolution over a field 4° x 3° in this direction show up to four HI line components. Two, near 0 and -50 km s^{-1}, are ubiquitous; their combined column density is always $\geq 4.5 \times 10^{19}$ cm^{-2}. There is also a narrow component at -10 km s^{-1} attributable to a diffuse cloud covering half of the field, and scattered patches of HI at $v < -100$ km s^{-1}. The low and intermediate velocity components have a broad line width and are so smoothly distributed across the region that it is unlikely that they contain significant unresolved angular structure. Eight other low column density directions were also observed. Their spectra typically have several components, but the total column density is always $> 7 \times 10^{19}$ cm^{-2} and changes smoothly along a 2° strip. Half of the directions show narrow lines arising from weak diffuse HI clouds that contain $0.5\text{-}3.0 \times 10^{19}$ cm^{-2}.

Directions north of declination -40° that have $N_{HI} < 7 \times 10^{19}$ cm^{-2} appear to be quite rare, and it is unlikely that the HI column density ever drops significantly below 4.5×10^{19} cm^{-2} anywhere in the sky. Thus the ISM provides an effective barrier to the direct passage of ionizing radiation at $E < 100$ eV, either from extragalactic sources into the galactic plane, or from the solar neighborhood into the galactic halo.

I. INTRODUCTION

This paper contains the first results of a study of HI emission in the regions of the northern sky that have the least neutral hydrogen. These areas are of particular interest because they often have so little HI that spectra can be decomposed, with confidence, into a few individual features that persist over degrees. This is very different from the situation in directions where HI is plentiful and spectra are obviously a confused blend. We hope that the low column density regions will provide a starting point for understanding the small-scale organization of the interstellar medium. Our second goal, and one that is stressed in this paper, is to search for directions that might have extremely small amounts of neutral hydrogen and thus provide transparent lines of sight to extragalactic objects at EUV and soft X-ray wavelengths.

Low HI column density directions were chosen guided by the HI survey of Stark et al. (1986; hereafter SBLH), which was made with the Crawford Hill horn-reflector of the AT&T Bell Laboratories. This survey has an angular resolution of only ~ 3° x 2°, but it is uncontaminated by stray radiation and thus able to supply large-scale HI column densities more accurately than previous studies. Our primary target was the region around ℓ = 150°, b = 53°. It has the lowest column density in the SBLH survey, and, because it appears as a local hole in column density maps, we refer to that area as "The Hole." Other directions studied include ℓ = 86°, b = 76°, the second lowest N_{HI} region in the SBLH survey, the north and south galactic poles, and several regions which were found to have a low total N_{HI} in the course of observing > 100 high latitude directions (Jahoda et al. 1985; Lockman, Hobbs and Shull 1985).

The areas that were observed are listed in Table 1 with their $\langle N_{HI} \rangle$ over the SBLH beam. Our higher resolution 21' observations have revealed a few directions with a total N_{HI} of only 4.5×10^{19} cm^{-2}, the lowest ever reported in galactic 21 cm studies, but in general, directions with $N_{HI} < 7 \times 10^{19}$ cm^{-2} seem quite rare.

Accurate measurement of low brightness galactic HI profiles requires that stray radiation be removed from the spectra. The technique used for this, and a discussion of ways to improve the correction for instrumental baselines, are given in Appendices.

II. OBSERVATIONS AND DATA REDUCTION

All of our 21 cm data were obtained with the 43 m (140 foot) telescope of the NRAO in Green Bank, West Virginia, during April 1984. At the frequency of the 21 cm line this telescope has a half-power beam-width (HPBW) of 21'. The receiving system consisted of dual cooled FET amplifiers and a hybrid mode feed that gave simultaneous linear polarizations (Norrod 1984). The total system temperature, on the telescope at zenith, was 23 K, the aperture efficiency was 60% and the main beam efficiency was about 80%. Spectra covered ± 240 km s^{-1} about zero velocity LSR at a resolution of 1.0 km s^{-1}.

A parabolic baseline was removed from each spectrum using a technique described in Appendix B. The noise in the final spectra is typically < 0.07 K (T_b) and a typical error in a column density determination, including baseline uncertainties, is 5×10^{18} cm^{-2}. Column densities were derived under the assumption that the lines are optically thin. This is a good assumption, as the peak line temperatures are always < 3.5 K (T_b) and typically < 2.5 K.

One-dimensional maps of the HI distribution were made by measuring spectra every 10' in right ascension along 2° strips at constant declination. Toward The Hole a number of strips were combined to give complete coverage of an area 4° x 3° at 10' x 10' spacing.

The treatment of stray radiation is discussed in detail in Appendix A. In brief, an area including the entire main beam of the Crawford Hill horn-reflector of AT&T Bell Labs was mapped with the 43 m telescope. This map was convolved with the horn-reflector beam pattern, and differences between the convolved 43 m spectra and that actually observed using the Bell Labs antenna (SBLH) are interpreted as arising from stray radiation which is then removed from individual 43 m spectra. The stray radiation correction was

redetermined at least every 1.5 hours and independently for every direction. We are confident that the accuracy of the resultant spectra is limited by noise and uncertainty in the instrumental baseline rather than by stray radiation.

III. THE HOLE

Figure 1 shows the low column density end of the SBLH HI survey binned by the total column density in each spectrum. Of the ~ 22000 spectra in that survey, which covers $\delta > -40°$, only 0.9% have a total HI column density $< 1 \times 10^{20}$ cm^{-2}, and directions with $N_{HI} < 7 \times 10^{19}$ cm^{-2} comprise < 0.1% of the survey. These lowest column densities (shaded portion of the figure) all come from a part of the sky centered roughly on $\alpha = 10^h.7$, $\delta = 58°$. We call this region "The Hole."

a) The Total Column Density

A map of the integrated HI column density over ~12 square degrees of The Hole is shown in Figure 2. The map is centered at $\alpha_{1950} = 10^h\ 45^m$, $\delta_{1950} = +57°\ 20'$. Within the area of complete coverage (indicated by the dashed border) spectra were taken every 10' in both coordinates. Each position was observed at least twice; a total of about 1300 spectra were combined to make the map. The contour levels are in units of 10^{19} cm^{-2} and the minimum N_{HI}, 4.5×10^{19} cm^{-2}, is observed at offset position -60', 0' and again near +75', +50'. In retrospect, the map should have been extended to lower right ascension, but the observed spectra were all heavily contaminated by stray radiation (see Appendix A) so there was no way to know what the true signal was during the observations. Nonetheless, we have a few additional spectra outside the borders of Figure 2 which indicate that the main minimum in N_{HI} is covered in our survey. Therefore, in all likelihood, Figure 2 shows the smallest HI column density directions north of declination -40°.

The HI spectra toward The Hole are remarkably simple. Examples are given in Figure 3 identified by their offset positions for reference to the map in Figure 2. Each spectrum can be decomposed into at most four well-defined

Gaussian components, and Figure 2 was derived from summing their individual contributions. The component with the largest column density is broad and near zero velocity. Every spectrum also contains another broad line at an intermediate velocity near -50 km s^{-1}. These two components contain most of the column density in The Hole. In some directions the spectra show a third component that is a bright narrow line attributable to a diffuse HI cloud. It covers about half of the region. The fourth, high velocity, component shows up as occasional weak emission at $v < -100$ km s^{-1} that is never brighter than the example shown in Figure 3.

The spectrum from offset (-65',0') shown in Figure 3 is the weakest galactic HI line detected to date, both in terms of peak brightness temperature (0.6 K T_b) and total N_{HI} (4.5×10^{19} cm^{-2}). Nonetheless it contains two distinct components and both have a line width (FWHM) ~25 km s^{-1}.

b) The Individual Components

Column density maps for the spectral components are given in Figure 4. The low velocity emission is the most uniform spectral feature over The Hole. It contains half or more of the total N_{HI} nearly everywhere inside of the mapped region. Its column density never falls significantly below 3×10^{19} cm^{-2} even over the broad minimum that runs diagonally across the map, and it reaches a maximum of just over 4.5×10^{19} cm^{-2} at the edges of the map. Its peak brightness temperature ranges between 0.5 and 0.8 K, while its width (FWHM) is always close to 30 km s^{-1} and has no significant trend across the map. The column density structure thus reflects mainly changes in the peak temperature. Over most of the map the peak velocity is close to -2 km s^{-1}.

There is a trend to lower velocities, but by only a few km s^{-1}, in a roughly triangular area whose apex is near offset 0,0 and whose base extends over most of the bottom of the map.

The intermediate velocity component is also ubiquitous. Its minimum column density is only slightly less than 1 x 10^{19} cm^{-2} while its maximum is slightly greater than 3 x 10^{19} cm^{-2} at the map edge. The average line width is about 30 km s^{-1}, but it decreases roughly with right ascension from about 35 km s^{-1} at the right edge of the map to about 22 km s^{-1} at the left edge. Most of the column density structure is caused by changes in the peak line temperature which ranges between 0.2 and 0.7 K. In a few directions this intermediate velocity feature is as bright as the low velocity feature, but it always has less column density. The peak velocity varies from about -45 km s^{-1} at low right ascension to about -51 km s^{-1} at high right ascension but with considerable scatter within these limits. The velocity gradient is opposite to the sense of galactic rotation.

The location of the cloud is shown in Figure 4, and maps of its line width and peak velocity are shown in Figure 5. Column density contours are in 10^{19} cm^{-2}, and the line width and velocity contours are in km s^{-1}. The dashed contour shows the extent of the minimum detectable emission. The cloud consists of northern and southern parts that are joined by faint emission. The northern part ($\Delta\delta > -30'$) has a narrow line width: it is usually <6 km s^{-1} and occasionally drops slightly below 4 km s^{-1}. There is also a gradient in line width across the northern part: Δv generally increases with right ascension and is larger at the cloud edge than near the center. The line width of the southern component is much larger with a stronger gradient. The width is always > 6 km s^{-1} and rises to just over 14 km s^{-1}. The two cloud

components also differ in their velocity. The northern component has a slight east-west gradient of a few km s^{-1}, while the velocity of the southern component decreases rapidly to the southeast. It is possible that the southern component is actually a superposition of two small clouds.

Even though the column density in the cloud peaks in the areas where the main low velocity feature is also strongest, there is no clear connection between these two spectral components. The velocity and line width gradients in the cloud have no counterpart in the low velocity emission, and the cloud always has a more negative velocity by up to 10 km s^{-1}.

The cloud is much fainter than typical diffuse HI clouds which have column densities $\sim 2 \times 10^{20}$ cm^{-2} (e.g., Spitzer 1978), but is very much like the "cloudlets" discovered by Heiles (1967). If it is ~100 pc away, then it is only a few pc across and has a mean density ~1 cm^{-3}.

High velocity emission over The Hole is weak and scattered. Its column density (Fig. 4) is never much more than 1×10^{19} cm^{-2}. Dashed contours mark the maximum but uncertain extent of the high velocity patches. Most of the gas has a velocity of about -105 km s^{-1} except in the northeast corner of the map where the velocity is near -130 km s^{-1}. Line widths are about 25 km s^{-1} and the peak brightness temperature is never greater than about 0.2 K. Clouds at similar high velocities have been reported in this general part of the sky (e.g., Giovanelli 1980).

c) Spatial Structure in the Emission

The dominant HI components toward The Hole look very smooth in the column density maps. A quantitative measure of smoothness is the first order structure function D:

$$D(\theta) \equiv \frac{1}{n} \sum_{n} [N_{HI}(i) - N_{HI}(i+\theta)]^2 \qquad (1)$$

where θ is an angular separation and the sum is over the n appropriate spectra in the map (see, e.g., Rutman 1978; Simonetti, Cordes, and Heeschen 1985). The first order structure function gives the mean square difference in N_{HI}, over the entire map, of points separated by the angle θ. Because our map is sampled every 10' while the 43 m beam is 21', the structure function for θ = 10' should contain almost entirely noise and baseline uncertainties which are unrelated to the spatial emission structure, i.e., $D(10') \approx 2\sigma^2$. The uncertainty in a total column density, estimated this way, is $\sigma = 0.4 \times 10^{19}$ cm^{-2}, which is about what is expected from our error analysis (§II). It thus makes sense to define a reduced structure function $D'(\theta) \equiv [D(\theta) - D(10')]^{1/2}$ which contains mainly information on the spatial variations in N_{HI}. Figure 6 shows D' for the total N_{HI} and for the dominant low and intermediate velocity components, normalized by the typical column density of each: 5.5×10^{19} cm^{-2}, 3.5×10^{19} cm^{-2}, and 2×10^{19} cm^{-2}, respectively. This figure thus gives the proportional average rms difference in column density over a given angular scale. It shows that nearby points are highly correlated, distant points less so.

The fact that D' (θ) is nearly monotonic confirms what the appearance of the column density maps suggests--that the column density changes are dominated by gradients, not by relatively small scale irregularities. The apparent detail in the total column density map is somewhat misleading in this regard, for what is not readily apparent there, but shows up in the structure function analysis, is that there is always an underlying constant N_{HI}; the maximum difference between any two points in the map is always less than a factor of 2, and is usually less than a factor of 1.25. Although the intermediate velocity component can show fluctuations of up to 40% at large

scales, the low velocity, and dominant, component is quite smooth on small scales. For these reasons, and because most of the column density is in components that have a line width ~25 km s^{-1}, we think that significant structure in the total N_{HI} on angular scales smaller than those observed here is unlikely. This issue is discussed further in the following section.

IV. OTHER LOW N_{HI} DIRECTIONS

Neutral hydrogen observations, corrected for stray radiation, were made in right ascension strips 2° wide across eight areas of low N_{HI} in addition to The Hole. Figure 7 shows the distribution of N_{HI} for these strips, and Figure 8 gives the spectrum at the center of each strip. One common characteristic of every field is that the emission varies smoothly and has no local peaks or holes. In the example of greatest emission variation, the strip centered at $l = 182°$, $b = +58.^{\circ}4$, much of the change is caused by structure in a well known high velocity cloud that lies in this direction (e.g., Giovanelli 1980). The dashed line in the N_{HI} curve for this strip shows the hydrogen omitting the contribution from the HVC. None of the eight areas ever has an $N_{HI} < 7 \times 10^{19}$ cm^{-2}.

The spectra always contain one or more broad components and often a relatively narrow, bright line like that from the cloud which covers part of The Hole. These "clouds" have column densities in the range 0.5 to 3.0×10^{19} cm^{-2}, linewidths (FWHM) of 4–12 km s^{-1} and velocities between −15 and +1 km s^{-1}. They cover about half of the low N_{HI} directions. These relatively weak features, which would be difficult to disentangle from the bright HI emission in more typical high-latitude directions, seem to pervade the interstellar medium. As in The Hole, these clouds are not obviously connected with the main low velocity gas.

The general HI structure in regions of low N_{HI} can be described by several statistics. For each strip we have calculated the mean N_{HI} and its dispersion σ. The ratio $\sigma / \langle N_{HI} \rangle$ ranges between 2.3% and 11.5% with an average value of 7.2%. The reduced and normalized structure function, $D'(\theta)$, as described in §IIIc, averages 0.10 ± 0.06 at $\theta = 60'$ and 0.15 ± 0.09 at $\theta = 90'$. Values of D' for the total N_{HI} in the Hole (Fig. 6) are within the 1σ range of these

results. Some directions are remarkably smooth in total N_{HI}. The strips centered at 56°.0 + 66°.1 and 85°.6 + 75°.9 have $\sigma/\langle N_{HI}\rangle$ of 2.3% and 3.7%, respectively; toward 56°.0 + 66°.1, where the total N_{HI} is always $< 1 \times 10^{20}$ cm^{-2}, the reduced structure function $D'\langle 60'\rangle = D'\langle 90'\rangle = 0.02$. Even the cases of most extreme spatial variation, the south galactic pole and 182°.0 + 58°.4, have a $\sigma/\langle N_{HI}\rangle$ that is only 11.5% and 11.1%, respectively.

Another perspective on the essential smoothness of N_{HI} in these areas comes from comparison of $\langle N_{HI}\rangle$ over the ~ 0.7 square degrees of our strips with the average over the ~ 6 square degrees of the SBLH survey beam (Table 1). For the eight areas the average ratio of our column densities to those of SBLH is 1.01 ± 0.09 (1σ). The maximum difference in column density between a single spectrum at 21' resolution and one at ~3° x 2° resolution is 5.8×10^{19} cm^{-2}, and this is caused by a small high velocity cloud in the 21' spectrum. If high velocity gas is neglected, then the maximum difference is half this value, only 3×10^{19} cm^{-2}. In low N_{HI} directions only HVC's are significantly clumped on angular scales < 2°, and coarse resolution surveys provide a good guide to the total column densities seen at higher resolution, within a 1σ uncertainty of ~10%. A similar strong correlation in N_{HI} between high latitude positions separated by 8° has been observed by Payne, Salpeter, and Terzian (1983).

These considerations suggest that the hydrogen is extended and not contained in very small, unresolved, clouds. For example, there would have to be ~ 100 small clouds in the ~ 0.2 square degrees of the 43 m beam to produce the observed $\sigma/\langle N_{HI}\rangle$ ~ 0.1. At a distance of 100 pc, each would have a diameter ~ 0.1 pc and a density $\langle n\rangle$ ~ 200 cm^{-3}.

V. SUMMARY

Areas of low total neutral hydrogen at $\delta > -40°$ have a number of common features:

1. Directions with $N_{HI} < 7 \times 10^{19}$ cm^{-2} are rare. We have found only one such area: The Hole near $\ell = 150°$, $b = 53°$. Even there the column density is $> 5 \times 10^{19}$ cm^{-2} except over two small regions where it reaches 4.5×10^{19} cm^{-2}.

2. The total column density, even in these low N_{HI} regions, varies quite smoothly with position. A typical rms dispersion in N_{HI}, for all points in a 2° long strip, is only 10% of the mean. The rms difference between column densities 1° apart on the sky is < 15% of the mean. In regions of low N_{HI} the smallest angular scale features are high velocity clouds. These contribute most of the small-scale structure in some directions. The part of The Hole at offset (-45', -50') in Figure 2 is one such example, as is the area around 182°.0 + 58°.4 (Fig. 8). Large changes in N_{HI} with position typically arise from broad gradients, as emphasized by Payne, Salpeter and Terzian (1983), and not from small-scale fluctuations. Thus observations at the rather coarse angular resolution of ~3° x 2° (Stark et al. 1986) give a good estimate of the total HI which would be seen at higher resolution.

3. Profile shapes in low N_{HI} regions are usually complex. Most show between three and five components over a few degrees of the sky. But most of the emission is in broad spectral features with a FWHM > 25 km s^{-1} that change smoothly with position.

4. About half of the low N_{HI} directions, including The Hole, show a relatively narrow spectral component with a FWHM between 4 and 12 km s^{-1}, like that expected from a small diffuse cloud. The features contain $0.5\text{-}3.0 \times 10^{19}$ cm^{-1} and have velocities $-15 < v < 1$ km s^{-1}. They do not seem

to be simply connected with the main, broad, low velocity emission lines. These weak, narrow features would be difficult to detect in the brighter and more confused HI profiles that are typical of most of the sky. They are probably the faint end of the "cloudlet" population discovered by Heiles (1967).

Although our observations are limited to $\delta > -40°$, it is likely that they cover the lowest N_{HI} directions anywhere. The all-sky HI data of Cleary, Heiles and Haslam (1979), which contain varying amounts of stray radiation, still show a number of directions at $\delta > -40°$ with $N_{HI} < 1 \times 10^{20}$ cm^{-2}, but no such directions south of $-40°$. It therefore seems probable that column densities significantly less than our minimum, 4.5×10^{19} cm^{-2}, do not exist in any direction, and that the interstellar medium is opaque ($\tau > 2$) to extragalactic radiation at energies between 14 and 100 eV.

This research was supported in part by the National Aeronautics and Space Administration under grant NAG 5-629. We are grateful for the use of the Midwest Astronomical Data Reduction and Analysis Facility (MADRAF).

APPENDIX A

CORRECTION OF 21 cm SPECTRA FOR STRAY RADIATION

Radio telescopes have weak sidelobes that cover the entire sky. Neutral hydrogen emission entering these sidelobes adds to emission detected via the main beam. When the main beam lies on an area of weak HI while the sidelobes cover bright emission from the galactic plane, the "stray" radiation can comprise half of the observed signal. This problem has been recognized for some time (e.g., Van Woerden, Takakubo and Braes 1962), and elaborate methods have been devised to reduce or remove its influence (e.g., Kalberla, Mebold, and Reich 1980; hereafter KMR).

Figure 9 shows an example of the problem. These two spectra were obtained with the NRAO 43 m telescope at Green Bank from identical observations of identical parts of the sky at two different hour angles. The 43 m telescope is equitorially mounted, so when it tracks an object its sidelobe pattern is fixed with respect to the sky. Even so, the stray radiation changes as far sidelobes move above and below the horizon. This, together with the fact that stray radiation enters a spectrum at a velocity which is not reduced to the LSR, means that the stray radiation spectrum is a function of telescope hour angle and elevation, and the time of year. But, as emphasized by KMR, the time varying component of stray radiation, which is so prominent in Figure 9, is only a lower limit to the total amount.

Stray radiation can be removed from a spectrum through an all-sky deconvolution provided that the complete antenna response pattern is known to below the -50 dB level. This method was used by KMR, who modelled the far sidelobes of the 100 m Effelsberg telescope to the -70 dB level (the far sidelobes of most antennas cannot, in general, be measured accurately) and

estimated a stray radiation spectrum by convolving the antenna pattern with the $\approx 2 \times 10^5$ spectra in the Weaver and Williams (1973) and Heiles and Habing (1974) HI surveys. We found this technique unattractive primarily because the far sidelobe pattern is sensitive to the illumination pattern and geometry of a telescope. Any change in the receiver feeds, or the telescope structure, would require a laborious recalculation of the sidelobe response. Such changes, particularly in the form of receiver improvements, occur routinely at Green Bank.

Some radio telescopes, such as horns and horn-reflectors, have negligible far sidelobes and hence little or no stray radiation. One such instrument is the Crawford Hill horn-reflector of the AT&T Bell Laboratories (hereafter the BL telescope) which was used recently for an HI survey of the northern sky (Stark et al. 1986; hereafter SBLH). Although this survey has minimal stray radiation, the telescope has an angular resolution of only $\sim 3° \times 2°$ at 21 cm; for many purposes HI needs to be measured on smaller angular scales.

We have developed a method of "bootstrapping" 43 m HI spectra to the SBLH survey which yields data at 21' resolution uncontaminated by stray radiation. The method has been used for several years with receivers having quite different illumination patterns, and it gives repeatable, reliable results.

This Appendix contains all the information that is necessary to use the method on any telescope. Section a) describes the technique and the fundamental assumptions on which it rests. Section b) contains a discussion of the BL antenna and of the assumption that the SBLH survey data have no significant stray radiation. In section c) we discuss the methodology of the observations, and show, in d), the typical levels of stray radiation that are present in 43 m spectra. Extensive tests of the other basic assumptions are

reported in section e) and in f) we summarize the technique and discuss its limitations.

a) The Technique

In principle, a high angular-resolution map made with a large filled-aperture telescope (the NRAO 43 m) can be convolved with the beam pattern of a smaller telescope (the BL horn-reflector) to reproduce the low-resolution observations exactly. We use this fact to interpret any differences between a convolved 43 m spectrum and the one observed at BL as originating in stray radiation in the 43 m data. Heiles (1974) made similar calculations in a few directions to determine a rough stray radiation correction to the Heiles and Habing (1974) HI survey.

The stray radiation spectrum, $\langle S(v, \alpha_0, \delta_0)\rangle$, averaged over $\sim 3° \times 2°$ toward a particular direction at a particular time, is defined as

$$\langle S(v,\alpha_0,\delta_0)\rangle = \langle T_{NRAO}(v,\alpha_0,\delta_0)\rangle - T_{BL}\ (v,\alpha_0,\delta_0), \qquad A1$$

where

$$\langle T_{NRAO}(v,\alpha_0,\delta_0)\rangle = \int_{\Omega} T_{NRAO}(v,\alpha,\delta)\ f(\alpha-\alpha_0,\delta-\delta_0)\ d\Omega, \qquad A2$$

the $T_{NRAO}(v,\alpha,\delta)$ are spectra from a map made at the 43 m, $T_{BL}(v,\alpha_0,\delta_0)$ is the spectrum observed by SBLH, and $f(\alpha-\alpha_0,\delta-\delta_0)$ is the antenna pattern of the BL horn-reflector normalized so that

$$\int_{\Omega} f(\alpha-\alpha_0,\delta-\delta_0)\ d\Omega = 1. \qquad A3$$

The stray radiation spectrum is not only a spatial average over the BL beam, but an average over the time, Δt, required to obtain the 43-m spectra. If we assume that the stray radiation contribution is essentially constant over some area around (α_0,δ_0), and that it is constant over Δt, then the average stray

radiation spectrum derived from a 43 m map can be removed from individual spectra in that map to produce "corrected," high-resolution spectra:

$$T_{cor}(v,\alpha,\delta) = T_{NRAO}(v,\alpha,\delta) - \langle S(v,\alpha_0,\delta_0)\rangle. \qquad A4$$

The accuracy of $T_{cor}(v,\alpha,\delta)$ depends on the validity of three assumptions:

(1) That the BL telescope spectra are correct and contain no significant stray radiation. Note that all differences between $\langle T_{NRAO}\rangle$ and T_{BL} are transferred to T_{cor}. Those include noise, the instrumental baseline, and the relative calibration of the spectra.

(2) That the 43 m stray radiation spectrum has not changed significantly over the time, Δt, required to make the 43 m map.

(3) That the 43 m stray radiation spectrum does not change significantly over the area of the BL main beam, i.e. that $S(v,\alpha,\delta) = \langle S(v,\alpha_0,\delta_0)\rangle$ for $|\alpha-\alpha_0| < 1°$ and $|\delta-\delta_0| < 1°$.

Tests of the assumptions are described in detail in sections b) and e).

b) The BL Antenna and the SBLH Survey

The BL horn-reflector at Crawford Hill is described by Crawford, Hogg, and Hunt (1961). Its beam shape can be calculated from its far-field pattern, which has a directional dependence given by

$$\vec{E}(\theta_L,\theta_T) \propto i\int_{-\xi_0}^{\xi_0} d\xi \int_{-\phi_0}^{\phi_0} d\phi\ \vec{E}_s(\phi,\xi)\ \omega \exp[-i\omega\kappa\ (\cos\xi \sin\theta_L + \sin\xi \sin\theta_T)] \qquad A5$$

where $\omega = \cos\phi/(1-\sin\phi)$, $\kappa = 4\pi f/\lambda$, λ is the wavelength and f, the focal length of the reflector, is 20 feet (6.096 m). The integration is over the longitudinal and transverse angles within the horn, ϕ and ξ, respectively, between the half flare angles $\phi_0 = \xi_0 = 14.036$. Angles in the far field are

from the beam center in the plane containing the horn axis (θ_L) and the plane perpendicular to the horn axis (θ_T). For linear polarization the vector $\vec{E}_s(\phi,\xi)$ is the sum of four components, two in the longitudinal direction

$$\vec{E}_L = \cos\left(\frac{\pi}{2}\,\frac{\xi}{\xi_o}\right)\cos\xi\,\sin\gamma + \cos\left(\frac{\pi}{2}\,\frac{\phi}{\phi_o}\right)\sin\xi\,\cos\gamma \qquad \text{A6}$$

and two in the transverse direction

$$\vec{E}_T = \cos\left(\frac{\pi}{2}\,\frac{\xi}{\xi_o}\right)\sin\xi\,\sin\gamma + \cos\left(\frac{\pi}{2}\,\frac{\phi}{\phi_o}\right)\cos\xi\,\cos\gamma \qquad \text{A7}$$

where γ is the angle between the polarization in the horn and the $\phi = 0$ plane and is zero for purely transverse polarization.

The beam shape of the horn-reflector is a function of the antenna polarization and the HPBW varies from about 2°.9 x 1°.9 in transverse polarization to 2°.2 x 2°.4 in longitudinal polarization. The polarization angle of the SBLH survey varied systematically with elevation, being purely transverse at an elevation of 45°. Thus the antenna pattern must be calculated separately for each declination.

Almost all SBLH spectra were taken at transit; observations north of the zenith were usually made at an azimuth of 0°, south of the zenith at an azimuth of 180°. Thus θ_L and θ_T correspond to offsets in apparent α and δ, respectively, and the BL antenna pattern, $f(\alpha-\alpha_0,\ \delta-\delta_0)$, can be written

$$f(\alpha-\alpha_0,\ \delta-\delta_0) = \text{const.}\ \left|\vec{E}(\alpha-\alpha_0,\ \delta-\delta_0)\right|^2 \qquad \text{A8}$$

where the constant provides the normalization (eq. A2).

The calculated pattern does not deviate from the observed horn-reflector pattern (Crawford, Hogg, and Hunt 1961; Penzias, Wilson, and Encrenaz 1970) by more than a few percent, except that in longitudinal polarization

two far sidelobes, arising from spillover, and from diffraction over the drive wheel, appear at a level of up to -35 dB. The area under these far sidelobes is < 0.1% of that in the main beam. We estimate that in the worst case these far sidelobes could contribute as much as 8×10^{18} cm^{-2} to the observed column density, but a more typical value would be 0.5×10^{18} cm^{-2}.

More than 99% of the BL antenna response lies within 14° of the main beam, which itself contains 92% of the total response (Penzias, Wilson, and Encrenaz 1970). It would be a reasonably straightforward task to "correct" the SBLH survey for its own near sidelobes, but, it appears that these corrections would be insignificant in nearly all directions. For example, toward the minimum column density position in The Hole the correction for sidelobes within 14° of the main beam would be less than 2×10^{18} cm^{-2}, or about 4% of the uncorrected column density. This is an extreme case, because here the column density in the main beam is very low and all sidelobes lie on higher N_{HI} regions. The near sidelobe contribution to the SBLH survey thus seems insignificant.

The antenna response more than 14° away from the main beam, except for the unique spillover and diffraction lobes, is difficult to locate experimentally. Our calculations indicate that there should be two long, weak, sidelobes, extending east-west in longitudinal polarization and north-south in transverse polarization. If these lobes contained as much as 0.5% of the total response, we estimate that they could typically contribute 2×10^{18} cm^{-2} to the observed column density at high latitudes.

It appears that the stray radiation component of the SBLH survey should generally be less than a few times 10^{18} cm^{-2}, except for isolated instances where it might reach 1×10^{19} cm^{-2}. Thus, to a relatively high degree

of accuracy, we can treat the SBLH survey as if it had no sidelobes, and perform the convolution of the 43 m data (eq. A2) only over the area of the main BL beam.

c) Making the Observations

A 43 m map made over an elliptical area 5.°3 x 4° always covers the main BL beam to below the 10% response level and provides an adequate estimate of the BL spectrum. Moreover, a complete sample of this area at the 21' resolution of the 43 m, which would require ~ 550 spectra, is not even necessary. We have found that a total of 73 spectra distributed over the 5.°3 x 4° region are sufficient to give a convolved spectrum, $\langle T_{NRAO} \rangle$, that is accurate to 5×10^{18} cm^{-2} in integrated column density (see §Ae). With this large number of spectra, the signal-to-noise (S/N) ratio in $\langle T_{NRAO} \rangle$ is always very high even if only a little time is spent at each position. It thus makes sense to split the observations into two groups: target spectra, which are high S/N ratio data taken in the direction of interest before and after map spectra which are taken by rapidly scanning the area of the BL main beam closest to the direction of interest. The map spectra determine $\langle S \rangle$, using equation A1. The target spectra are the ones which are actually corrected via equation A4.

In section e) we discuss measurements of the rate of change of the stray radiation spectrum with time and position. The results indicate that target spectra can be observed for 30^m to 40^m before and after a map is made, and that it is generally desirable to center the map on a BL spectrum taken within 1° of the target positions.

d) Typical Stray Radiation Corrections for the 43 m

The 43 m spectra from Figure 9 are shown individually in Figure 10 along with the amount of each that is attributable to stray radiation (shaded

portions). There is so little HI in the main beam of the 43 m in this direction that the stray radiation is a particularly large fraction of the signal: about 57% of the observed upper spectrum and 48% of the lower spectrum can be attributed to stray radiation. Recall that both spectra are from the same direction, but were taken at different hour angles.

Observations at a number of high latitude directions were corrected for stray radiation. The integrated values of <S>, expressed as an equivalent HI column density, are plotted against the local sidereal time (LST) of observation in Figure 11. There is a large scatter in the amount of stray radiation, but it reaches a minimum around 12^h, when the galactic plane is at low elevations. The amount of stray radiation is not correlated with the total amount of hydrogen in the main beam.

Figure 11 shows that several spectra apparently have "negative" stray radiation, i.e., a signal that must be added to the 43 m spectra to bring them into line with the BL spectra. The effect occurs only when the signal is relatively large, and amounts to, at most, only 6% of the total column density. It probably arises from a combination of baseline and calibration differences. The 43 m data were calibrated by adopting the Williams (1973) values for the brightness of the standard regions S6 and S8. The SBLH temperatures were calibrated against a cold load and appear to be a few percent higher than the Williams values. When the stray radiation in a 43 m map is a negligible fraction of the total observed signal, either because the main beam emission is quite bright or because of the LST and attitude of the telescope, the quantity <S> in equation A1 contains only the calibration and baseline differences between the 43 m and SBLH observations; it can easily be negative. Further investigation of this phenomenon is in progress, but it

does not appear to cause a serious uncertainty in any of our data beyond the few percent level.

e) Tests of the Basic Assumptions

The two principal assumptions on which our correction procedure rests are (1) that the stray radiation spectrum does not change significantly over the time necessary to make the 43 m observations, and (2) that the stray radiation in a single 43 m spectrum is well approximated by the <S> determined over ~ 20 square degrees from the convolved 43 m map (eq. A4). These assumptions, and other observations designed to test the accuracy of our results, are discussed below.

i) Variation with Time

For the first test about 75 high-latitude directions were observed twice. In each case the second spectrum was taken about 40 min after the first. Differences between the spectra in a pair arise from noise, random baseline errors, and changes in the stray radiation component with time. The rms difference over the 75 pairs is only 4.0×10^{18} cm^{-2} to which noise and baseline errors contribute typically $< 2 \times 10^{18}$ cm^{-2}. The shape of the spectra did not vary significantly over this period.

As a second test, we produced three estimates of $\langle T_{NRAO} \rangle$ from consecutive maps centered on almost the same position. All maps were made from a set of right ascension strips separated by 30' in declination. Data were averaged over 2^s of time while the telescope was being driven in right ascension at either 90'/min (fast rate) or 30'/min (slow rate). A "slow" scan gives spectra every 10' in right ascension. A map at the fast rate was followed by one at the slow rate, offset 10' in declination, and then by another map at fast rate offset another 10' in declination. The entire procedure took about

two hours. Differences between the three resulting estimates of $\langle T_{NRAO} \rangle$ will be dominated by small angular scale structure in the HI, by time variations in $\langle S \rangle$, and by baseline uncertainties. These observations were made in 15 different directions. The maximum difference among the three values of $\langle T_{NRAO} \rangle$ for a given direction averaged only 5.2×10^{18} cm^{-2}, and was never larger than 1.2×10^{19} cm^{-2}. We conclude that $\langle S \rangle$ needs to be redetermined only every two hours or so, and that maps made at the fast rate, which contain just over 70 spectra, give an $\langle T_{NRAO} \rangle$ that is adequate for estimating the stray component in a 43 m spectrum.

ii) Variation with Position

The assumption that $\langle S \rangle$ derived over the ~3° x 2° area of the BL main beam is representative of the stray radiation over any smaller region within that beam is reasonable, for far sidelobes are always very broad (see, e.g., KMR).

We examined the variation in $\langle S \rangle$ that resulted from sequential observations of positions separated by 2°. Typical changes were $< 4 \times 10^{18}$ cm^{-2}, although a change of 2.6×10^{19} cm^{-2} was observed once. Over displacements of 4° to 10° the average difference in $\langle S \rangle$ was 1.2×10^{19} cm^{-2}. These differences include the effects of noise and baseline uncertainties as well as the changes in $\langle S \rangle$ over times ~1 hour.

Because these relatively large changes in position produce only modest changes in $\langle S \rangle$, we conclude that angular structure in $\langle S \rangle$ on scales < 2° is modest, and will introduce only minor uncertainties into our results.

iii) Internal Consistency

The most useful estimate of the internal consistency of the stray radiation correction process comes from maps of The Hole, where pairs of 43 m spectra, taken at sky positions separated by ≤ 5', but at times separated

by up to several days, were corrected using different BL spectra. The rms deviation of the difference in the corrected N_{HI} for 53 such pairs is 7×10^{18} cm^{-2}, giving an average error, per spectrum, of 5×10^{18} cm^{-2}. This error includes noise and baseline uncertainties, and is at most only 10% of the total column density. At high latitude positions more typical than The Hole, the error would be < 1% of the total N_{HI}.

In addition, the stray radiation correction procedure was applied to data from four observing sessions. Two of the sessions, during March and August 1983, used a receiver with dual linearly polarized scalar feeds. The other two sessions, in September 1983 and April 1984, used a receiver with dual linearly polarized hybrid-mode feeds. There was no significant polarization structure in the observed HI spectra, so data from the two polarizations were always combined. Many directions were observed in three sessions, and three directions in all four. These observations give a check on the consistency of the correction technique over time and with different antenna illumination patterns (and hence different main beam efficiency and sidelobes). Table A1 shows the average observed and corrected 43 m column densities for ten directions. The dispersion (1σ) on each N_{HI} is a measure of the total variation from all sources, including baselines and noise, over the sessions. The average dispersion in corrected spectra is 0.8×10^{19} cm^{-2} or < 4% of the average N_{HI}. The average corrected σ is close to the dispersion expected from noise and baseline uncertainties. For the average, and eight of the ten individual directions, $\sigma_{cor} < \sigma_{obs}$ indicating that the correction procedure has removed a stray component whose magnitude fluctuates from session to session. The stray radiation correction procedure thus gives spectra that are repeatable to a high degree of accuracy over several observing sessions and despite major equipment changes.

We conclude that the average error introduced by the assumption that the stray radiation spectrum is constant across 2-3 degrees in the sky and over a period of up to two hours is no greater than the 5×10^{18} cm^{-2} error in our data caused by noise and baseline errors. The maximum residual stray radiation error seems unlikely to be more than two or three times this value under any circumstance.

iv) Agreement with Other Determinations of N_{HI}

As discussed above, Kalberla, Mebold, and Reich (1980, hereafter KMR) have published HI profiles from the 100 m Effelsberg telescope that were corrected for stray radiation by a complete deconvolution of a model beam pattern using all-sky HI surveys. We observed two of the KMR directions; the corrected 43 m spectra at 21' resolution are compared with KMR spectra at 9' resolution in Figure 12. Toward KMR position 4 we find $N_{HI} = 7.3 \times 10^{19}$ cm^{-2} and KMR find 7.1×10^{19} cm^{-2}, in very good agreement, although the KMR spectrum has a slightly higher peak temperature. Toward the north galactic pole (KMR 17) we find 9.2×10^{19} cm^{-2} while KMR find only 6.7×10^{19} cm^{-2}. Most of the disagreement arises from the obvious baseline problems in the KMR spectrum; the profile shapes are in good agreement. Half or more of the observed signal has been removed from all four spectra in the stray radiation correction processes.

Additional support for our method comes from comparison of N_{HI} as derived from Lα observations of distant high-latitude stars with the corrected N_{HI} derived from 21 cm observations in the same direction. The six stars in the Lockman, Hobbs, and Shull (1985) survey that are expected to lie entirely beyond the galactic HI layer all show $N_{L\alpha} \approx N_{21}$ to within the observational uncertainties in $N_{L\alpha}$ ($\sim$ 15%). This agreement provides independent evidence that the overall 21 cm correction process gives accurate results.

f) Summary

This summary is based on our experience with the correction of ~5 x 10^4 high latitude HI spectra for stray radiation. In general, corrected HI column densities integrated over an entire spectrum should be accurate to ~1 x 10^{19} cm^{-2} (1σ) when all sources of error are included. Higher accuracy, by a factor of ~ 2, can be obtained in certain directions if special care is taken in the data acquisition and especially in baseline removal (see Appendix B). Also, because most stray radiation comes from relatively low velocity gas that is Doppler shifted by the combined earth-sun motion, spectral features at $|v| > 100$ km s^{-1} will usually not be contaminated and the accuracy of these is limited only by instrumental effects. We are continuing to study the stray radiation problem to refine the technique discussed here.

The limiting factors on this technique probably reside in the SBLH spectra. These were taken with a velocity resolution of only 5.3 km s^{-1}, so a narrow spectral line on the edge of a broad emission feature will appear shifted in velocity in their spectra. In extreme cases (of which we have a few examples), it is pointless to try to obtain corrected HI profiles at a velocity resolution higher than 5.3 km s^{-1}. Another limitation is that the SBLH survey covers only $\delta > -40°$; more negative declinations cannot be corrected for stray radiation. Nonlinearities in the SBLH filters (see SBLH) should not be a serious problem as these only affect bright lines in whose direction stray radiation is usually a very small fraction of the total signal. Finally, our technique assumes that the SBLH spectra are totally correct. From examination of a number of these spectra we estimate that any one may have an uncertainty that is equivalent to a column density error of 2 x 10^{18} cm^{-2} (1σ) caused primarily by baseline errors.

Stray radiation contributions to the SBLH profiles are estimated to be typically less than a few times 10^{18} cm^{-2}, and at most 1 x 10^{19} cm^{-2}, at intermediate and high galactic latitudes.

In summary, the method of "bootstrapping" high resolution spectra to the SBLH survey gives roughly an order of magnitude reduction in stray radiation over uncorrected high latitude HI spectra. This technique has the important advantage over a formal deconvolution of the antenna response (as done by KMR) in that it can be easily applied to any telescope, with any receiver, since detailed knowledge of the full antenna pattern is not required.

APPRENDIX B

REDUCTION OF ERRORS IN BASELINE REMOVAL

In the course of this project many thousands of HI spectra had to be corrected for instrumental baseline. The baseline is usually approximated by a low order polynomial which is fit, in the least-squares sense, to the emission-free channels of each spectrum. Because the polynomial is fit to noisy data, there are random errors in the derived coefficients which can be the dominant source of error in estimates of the power in a spectrum. This Appendix discusses a way to reduce the errors associated with baseline removal from sets of spectra.

The area, A, under a spectral line, is

$$A = \Delta v \sum_{L} (t_i - G_i) \qquad \text{B1}$$

where t_i is the observed temperature, G_i is the value of the polynomial baseline at the i^{th} channel, Δv is the channel spacing (taken to be unity from now on), and the subscript L indicates that the sum is over the spectral channels which may contain emission. If the polynomial G is simply a constant g_o, then

$$G_i \equiv g_o = \frac{1}{N_B} \sum_{B} t_i \quad , \qquad \text{B2}$$

where N_B is the number of channels that go into the baseline fit and the subscript B indicates that the sum is over these channels. If all channels are independent, and if each has the same variance σ_B^2, then the variance of g_o is given by

$$(\Delta g_o)^2 = \sigma_B^2 / N_B \quad . \qquad \text{B3}$$

In this case the area reduces to

$$A = \sum_{L} t_i - N_L \, g_0 \qquad \text{B4}$$

where N_L is the number of channels in the line, and the variance in the area follows from the law of propagation of errors:

$$\Delta A^2 = \sigma_L^2 \, N_L + \sigma_B^2 \, N_L^2/N_B \qquad \text{B5}$$

where σ_L^2 is the variance of a channel containing line emission. Because $\sigma_B^2 = \sigma_L^2$ and typically $N_B = N_L$, the uncertainty in the area has approximately equal contributions from noise in the signal and baseline regions of the spectrum.

Observations often require fitting higher order baselines, such as the second order polynomials removed from our HI spectra. To estimate the associated errors we write the baseline as an orthogonal polynomial

$$G_i = g_0 + g_1\beta + g_2 \, \gamma_1\gamma_2 \quad + \ldots \qquad \text{B6}$$

where $\beta = (i-\beta')$, $\gamma_1 = (i-\gamma_1')$, $\gamma_2 = (i - \gamma_2')$ and β', γ_1' and γ_2' are chosen to make g_0, g_1 and g_2 orthogonal (e.g. Bevington 1969). The quantities β, γ_1 and γ_2 are functions only of the channel number and baseline regions. An extension of equation B5 gives the variance in the area:

$$\Delta A^2 = \sigma_L^2 \, N_L + \sigma_B^2 \left(\frac{N_L^2}{N_B} + \frac{(\sum_L \beta)^2}{\sum_B \beta^2} + \frac{(\sum_L \gamma_1\gamma_2)^2}{\sum_B \gamma_1^2\gamma_2^2} + \ldots \right) \qquad \text{B7}$$

All terms in equation B7 are positive, so typically the uncertainty in the area is dominated by uncertainty in the baseline.

This analysis suggests that the variance of the area can be reduced if more channels are included in the baseline fit, i.e., if both the bandwidth and total number of channels in a spectrum are increased. This is often not

feasible, and even when it is, wide-band data generally need to be fit with a higher order polynomial baseline than narrow-band observations.

It is more useful to recognize that in removing an instrumental baseline we are attempting to model a function that typically changes slowly with time, and is usually highly correlated between spectra taken sequentially at nearby positions. A baseline model obtained from a fit to the average of n_s sequential spectra will have $\sigma_B^2 = \sigma_L^2/n_s$ and a more accurate ΔA as long as the true baseline is well behaved. This information is not used if spectra are reduced individually. For second-order baselines an $n_s \approx 3$ is usually sufficient to make the terms of equation B7 containing σ_B^2 smaller than the intrinsic uncertainty $N_L\ \sigma_L^2$. When $n_s > 1$ the baseline that is removed from any spectrum is not optimum in the least-squares sense, but differences tend to be small and well within the range of uncertainty of the least-squares solution.

The value of modeling the baseline from an average of n_s spectra was tested using the HI data obtained for this paper. Our original observing procedure was such that we took 13 sequential spectra spaced over a 2° strip on the sky. The strip was repeated about 45^m later, giving two spectra in each observed direction. The difference in area between the pairs of spectra gives a measure of the total uncertainty in the area from all sources. The average difference was attributed to a change in the stray radiation component. The dispersion arises from the baseline and noise. We reduced a hundred such pairs varying only the quantity n_s between tests. An $n_s = 1$ is the usual procedure of fitting a baseline to an individual spectrum. For $n_s = 3$ the baseline was fit to the average of three consecutive spectra and

then removed from the second spectrum of the triplet. An $n_s = 5$ was also tested. As $n_s \to \infty$, random baseline errors vanish and ΔA reaches its lowest possible value.

Table B1 shows the observed dispersion, ΔA, in K km s^{-1}, compared with the theoretical dispersion as given by equation B7. The technique of averaging consecutive spectra to reduce the error in the baseline clearly works for these data, and it gives dispersions in reasonable agreement with theoretical expectations. Improvement in the quality of the baselines for $n_s > 1$ is especially noticeable on video displays of spectral line maps.

This technique of spectrum averaging should be applicable to many different observations. The data presented in this paper were reduced with $n_s = 3$, and while an $n_s = 5$ did give some further reduction in ΔA, our conservative choice maximized the gain in accuracy while minimizing the chances that a real baseline change occurred over the n_s spectra. In all, some 13000 spectra were reduced this way with satisfactory results. Some care must be taken in using a large n_s with autocorrelation receiver spectra because these have $\sum t_i = 0$ as a result of normalization. Observations of strong lines with a lot of spatial structure may require use of an n_s no greater than 3 in these cases.

TABLE 1

OBSERVED DIRECTIONS

ℓ	b	α_{1950}	δ_{1950}	$\langle N_{HI} \rangle$ (10^{19} cm^{-2})
0°.0	+90°.0	$12^h49^m00^s$	+27°24'00"	9.9
56.0	+66.1	14 36 20	+34 08 32	9.7
85.6	+75.9	13 32 24	+38 10 04	7.8
100.7	+65.3	13 45 33	+49 33 44	11.4
133.3	−89.5	00 49 26	−26 52 00	15.8
150.5	+53.0	10 45 00	+57 20 00	5.9
160.0	+50.0	10 04 58	+53 53 59	7.6
182.0	+58.4	10 27 11	+39 10 53	13.9
199.8	+86.3	12 32 44	+28 10 45	14.6

. TABLE A1

Consistency of Corrected Spectra

ℓ,b	Sessions	-------N_{HI} (10^{19} cm^{-2})------ Obs.		Cor.	
35°-45°	3	38.1 ±	1.3	35.1	0.8
66 -45	3	53.3	1.0	48.1	0.4
68 -63	3	29.5	1.2	24.4	1.1
88 -30	3	61.5	3.6	49.8	0.1
101 +65	3	15.5	1.1	12.1	0.6
182 +58	4	17.7	1.2	14.0	0.6
214 -32	3	63.1	0.2	55.6	0.8
237 -27	4	30.1	1.9	19.7	0.9
240 +37	3	39.0	0.6	38.0	0.5
316 +51	4	22.8	1.6	23.6	2.3
		$\langle\sigma\rangle_{obs.}$ = 1.4		$\langle\sigma\rangle_{cor.}$ = 0.8	

TABLE B1

Dispersion in an Area Estimate Area Estimate

n_s	ΔA Theo. (K km s^{-1})	ΔA Obs. (K km s^{-1})
1	3.5	4.1
3	2.3	2.4
5	2.0	2.0
∞	1.4	...

REFERENCES

Bevington, P. R. 1969, Data Reduction and Error Analysis for the Physical Sciences, (New York: McGraw-Hill).

Crawford, A. B., Hogg, D. C., and Hunt, L. E. 1961, Bell System Tech. J., 44, 1095.

Cleary, M. N., Heiles, C., and Haslam, C. G. T. 1979, Astr. Ap. Suppl., 36, 95.

Giovanelli, R. 1980, A. J., 85, 1155.

Heiles, C. 1967, Ap. J. Suppl., 15, 97.

_____ 1974, Astr. Ap. Suppl., 14, 557.

Heiles, C. and Habing, H. J. 1974, Astr. Ap. Suppl., 14, 1.

Jahoda, K., McCammon, D., Dickey, J. M., and Lockman, F. J. 1985, Ap. J., 290, 229.

Kalberla, P.M.W., Mebold, U., and Reich, W. 1980, Astr. Astrop., 82, 275. (KMR)

Lockman, F. J., Hobbs, L. M., and Shull, J. M. 1985, Ap. J., (in press).

Norrod, R. D. 1984, NRAO Electronics Div. Internal Report No. 245.

Payne, H. E., Salpeter, E. E., and Terzian, Y. 1983, Ap. J., 272, 540.

Penzias, A. A., Wilson, R. W., and Encrenaz, P. 1970, A. J., 75, 141.

Rutman, J. 1978, Proc. IEEE, 66, 1048.

Simonetti, J. H., Cordes, J. M., and Heeschen, D. S. 1985, Ap. J., 296, (in press).

Spitzer, L. 1978, Physical Processes in the Interstellar Medium, (New York: Wiley).

Stark, A. A., Bally, J., Linke, R. A., and Heiles, C. 1986 (in preparation). (SBLH)

Van Woerden, H., Takakubo, K., and Braes, L. L. E. 1962, B.A.A.N., 16, 321.

Weaver, H. and Williams, D. R. W. 1973, Astr. Ap. Suppl., 8, 1.

Williams, D. R. W. 1973, Astr. Ap. Suppl., 8, 505.

FIGURE CAPTIONS

Figure 1. The distribution of the number of spectra in a given column density bin for the faint end of the SBLH HI survey. Of the ~22000 spectra in that survey, only 0.9% have a total $N_{HI} < 1 \times 10^{20}$ cm^{-2}, and < 0.1% have $N_{HI} < 7 \times 10^{19}$ cm-2. These lowest column density directions (shaded portion of the figure) all come from a part of the sky near $\alpha = 10^h7$, $\delta = 58°$, that we call The Hole.

Figure 2. The total HI column density toward The Hole. Positions are offsets from $\alpha = 10^h\ 45^m$, $\delta = 57°\ 20'$. Column density contours are in units of 1×10^{19} cm^{-2}. Spectra were measured every 10', in both coordinates, within the area outlined by the dashed border. The column density never drops significantly below 4.5×10^{19} cm^{-2} over this map.

Figure 3. Sample spectra toward The Hole showing the four line components. Offsets beside each spectrum refer to the scale in Figure 2. The spectrum at offsets (-65',0') is the weakest galactic HI line detected to date.

Figure 4. Column density maps for the individual spectral components toward The Hole. Contours are in units of 1×10^{19} cm^{-2}, and a dashed contour indicates the maximum (but uncertain) total extent of the emission. The positions are offsets from $\alpha = 10^h\ 45^m$, $\delta = 57°\ 20'$, as in Figure 2. The line components are defined in the text and illustrated in Figure 3. Note the smooth variation in column density for the dominant low and intermediate velocity components.

Figure 5. Line width (FWHM) and peak velocity maps of the cloud toward The Hole. Contours are in km s^{-1}.

Figure 6. The reduced structure function, D', versus angular separation, for the total N_{HI}, and for the N_{HI} in the low and intermediate velocity components toward The Hole. The figure shows the rms difference between column densities separated by θ, expressed as a fraction of the average column density in the component. It shows that nearby positions are highly correlated, and that the major structure is in gradients.

Figure 7. Column densities across eight low N_{HI} regions. Positions are offsets from the values given in Table 1. The dashed curve for the direction $\ell = 182°$, $b = 58.4$ shows the N_{HI} when the high velocity gas in this direction is not included. There are no column densities $< 7 \times 10^{19}$ cm^{-2}.

Figure 8. Spectra in the low column density areas. These were taken at the positions listed in Table 1, and are at the center of each strip in Figure 7. Note the complexity of the typical spectrum.

Figure 9. An example of the time variation of stray radiation. These spectra were taken at identical positions, but at two different hour angles. The varying component is only a fraction of the total stray radiation.

Figure 10. The same spectra as in Figure 9, along with the amount of each that arises from stray radiation (shaded areas). About 57% of the upper spectrum and 48% of the lower spectrum are attributable to stray radiation.

Figure 11. The amount of stray radiation, expressed as an equivalent column density of HI, that was removed from a number of high latitude observations, plotted against the LST of observation.

Figure 12. Comparison of spectra at 9' angular resolution from the 100 m telescope corrected for stray radiation by an all-sky deconvolution (labeled KMR with the running number assigned in that paper) with spectra at 21' resolution obtained at the 43 m and corrected by the method described in this Appendix. Before correction for stray radiation the spectra contained about twice the signal shown here. The agreement between the two methods is quite good, given the difference in angular resolution and the obvious baseline problems in the 100 m observations of KMR 17.

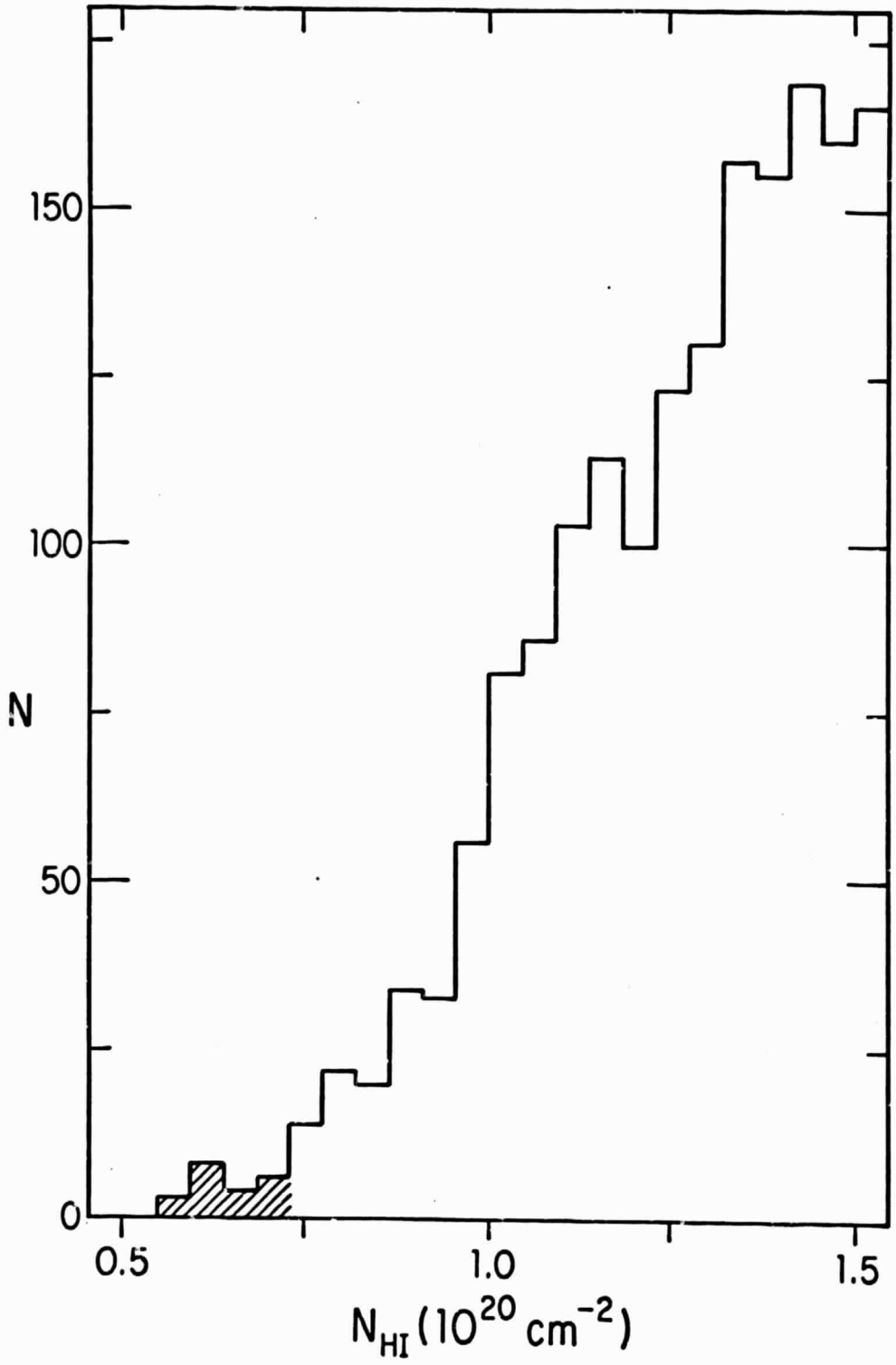

Fig. 1

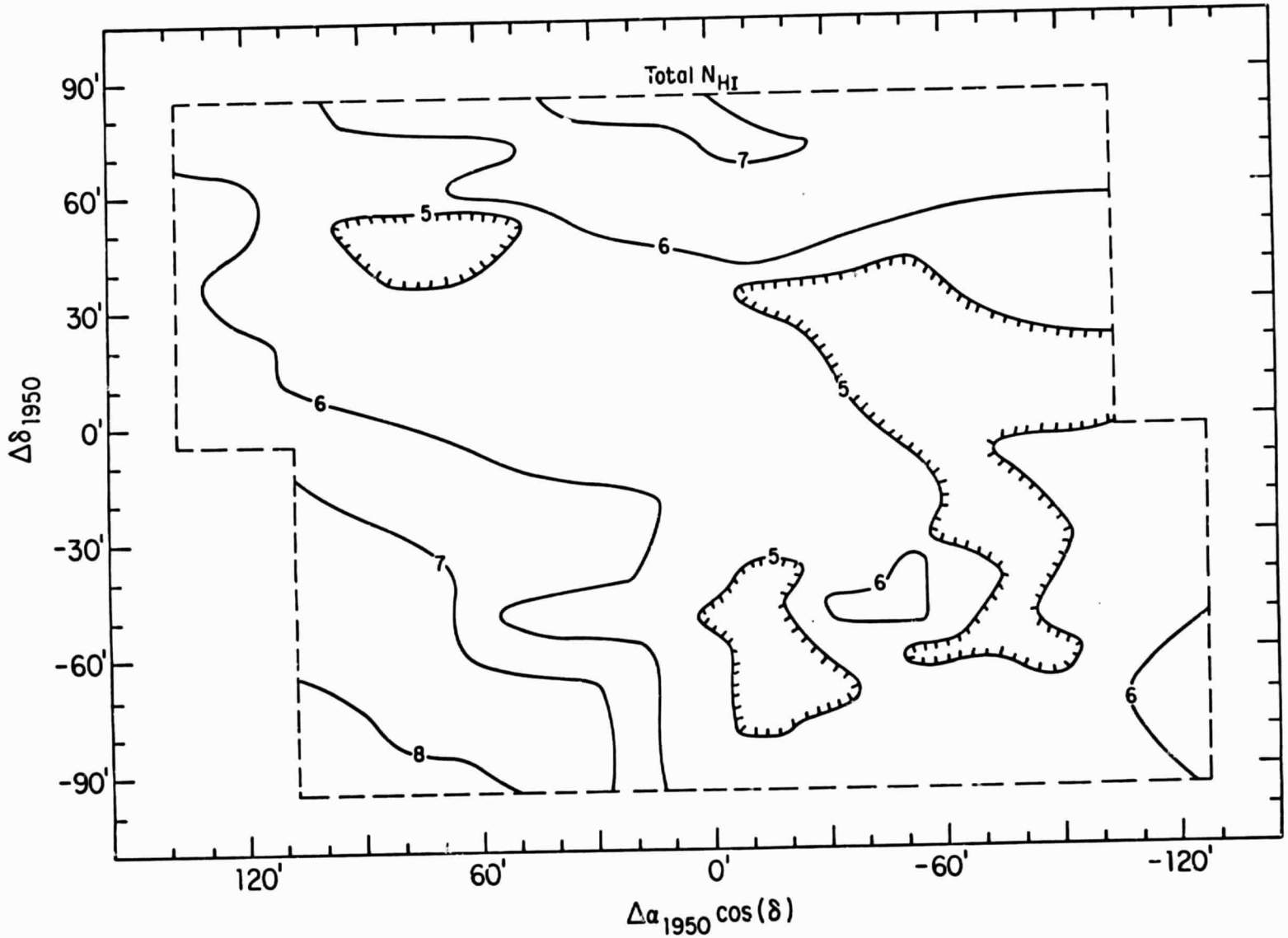
Total N_{HI}
90'
60'
30'
0'
-30'
-60'
-90'
$\Delta\delta_{1950}$
120'
60'
0'
-60'
-120'
$\Delta\alpha_{1950}\cos(\delta)$
5
6
7
8

Fig. 2

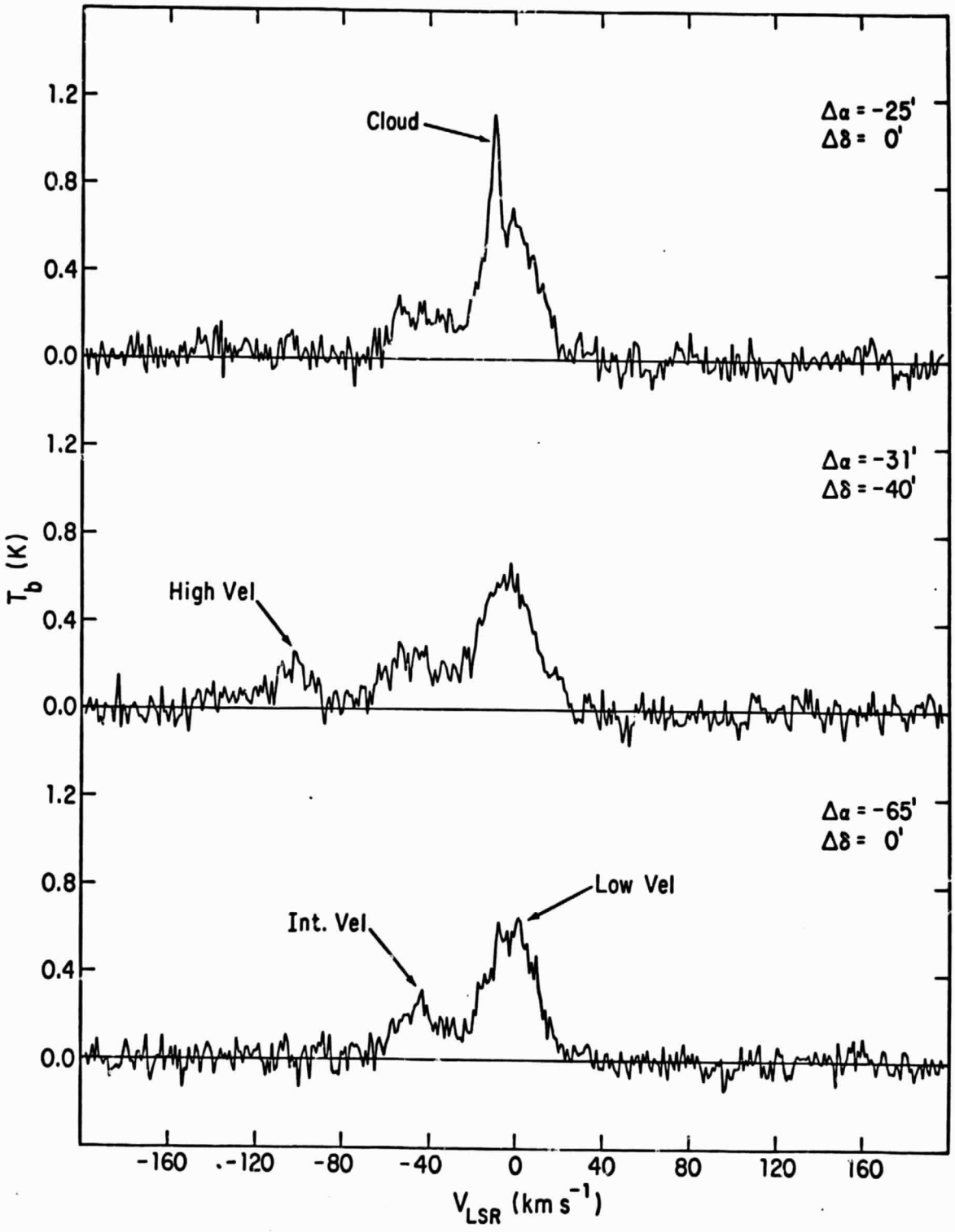
Cloud
Δα = -25'
Δδ = 0'
Δα = -31'
Δδ = -40'
High Vel
Δα = -65'
Δδ = 0'
Low Vel
Int. Vel
1.2
0.8
0.4
0.0
T_b (K)
-160
-120
-80
-40
0
40
80
120
160
V_LSR (km s^-1)

Fig. 3

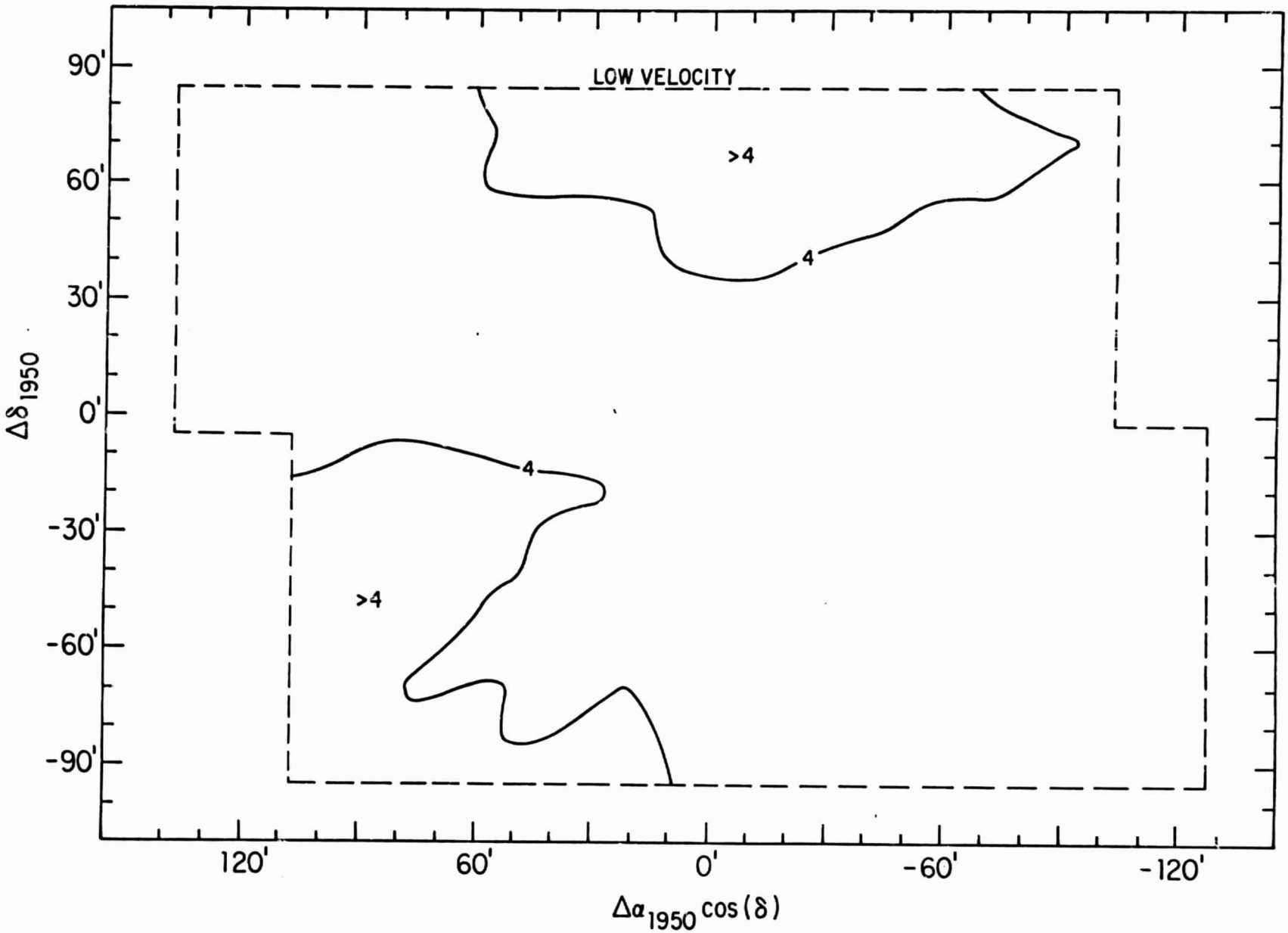
LOW VELOCITY
>4
4
4
>4
90'
60'
30'
0'
-30'
-60'
-90'
120'
60'
0'
-60'
-120'
$\Delta\delta_{1950}$
$\Delta\alpha_{1950}\cos(\delta)$

Fig. 4a

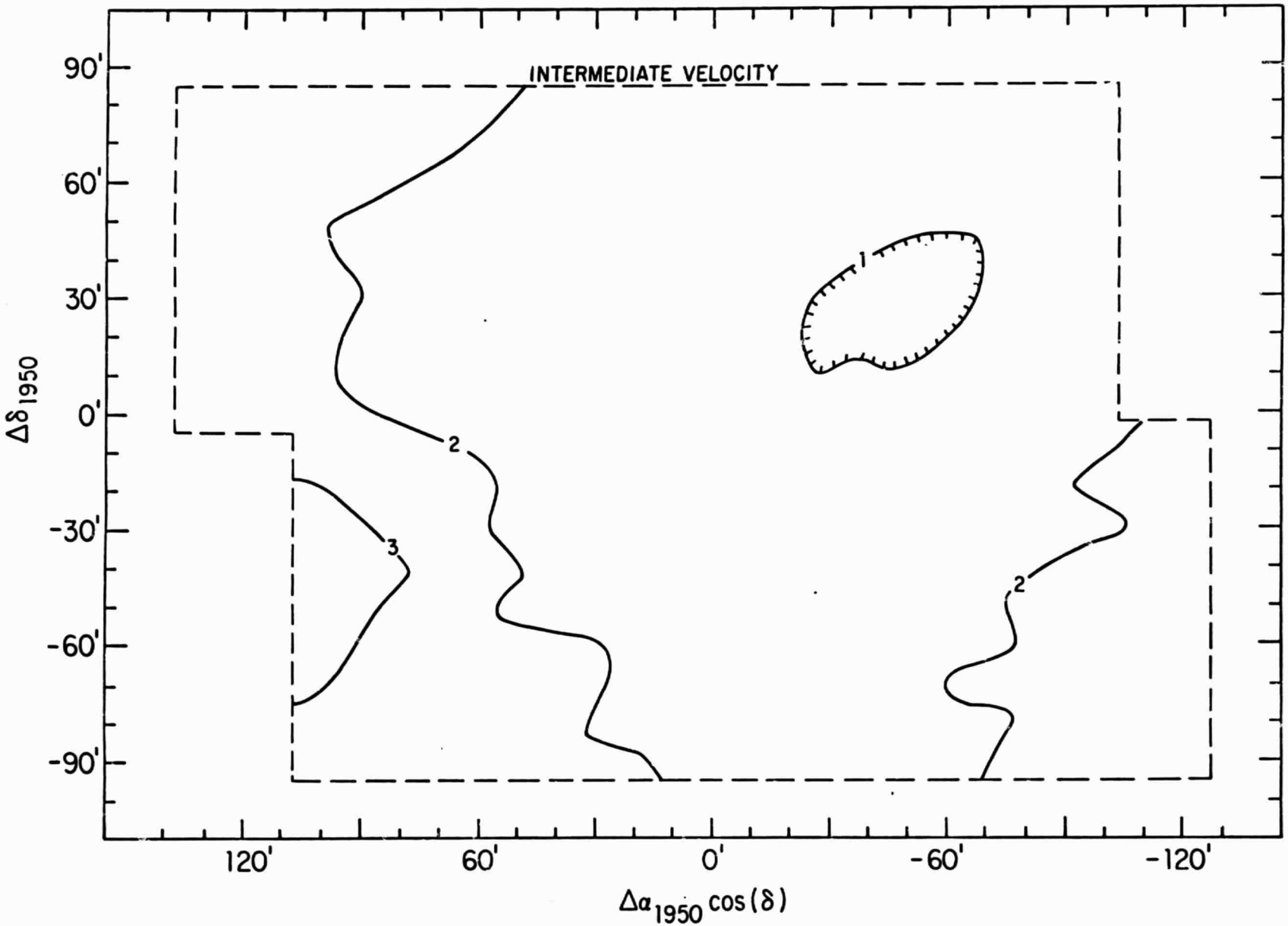
INTERMEDIATE VELOCITY
90'
60'
30'
0'
-30'
-60'
-90'
$\Delta\delta_{1950}$
120'
60'
0'
-60'
-120'
$\Delta\alpha_{1950}\cos(\delta)$
1
2
3
2

Fig 4b

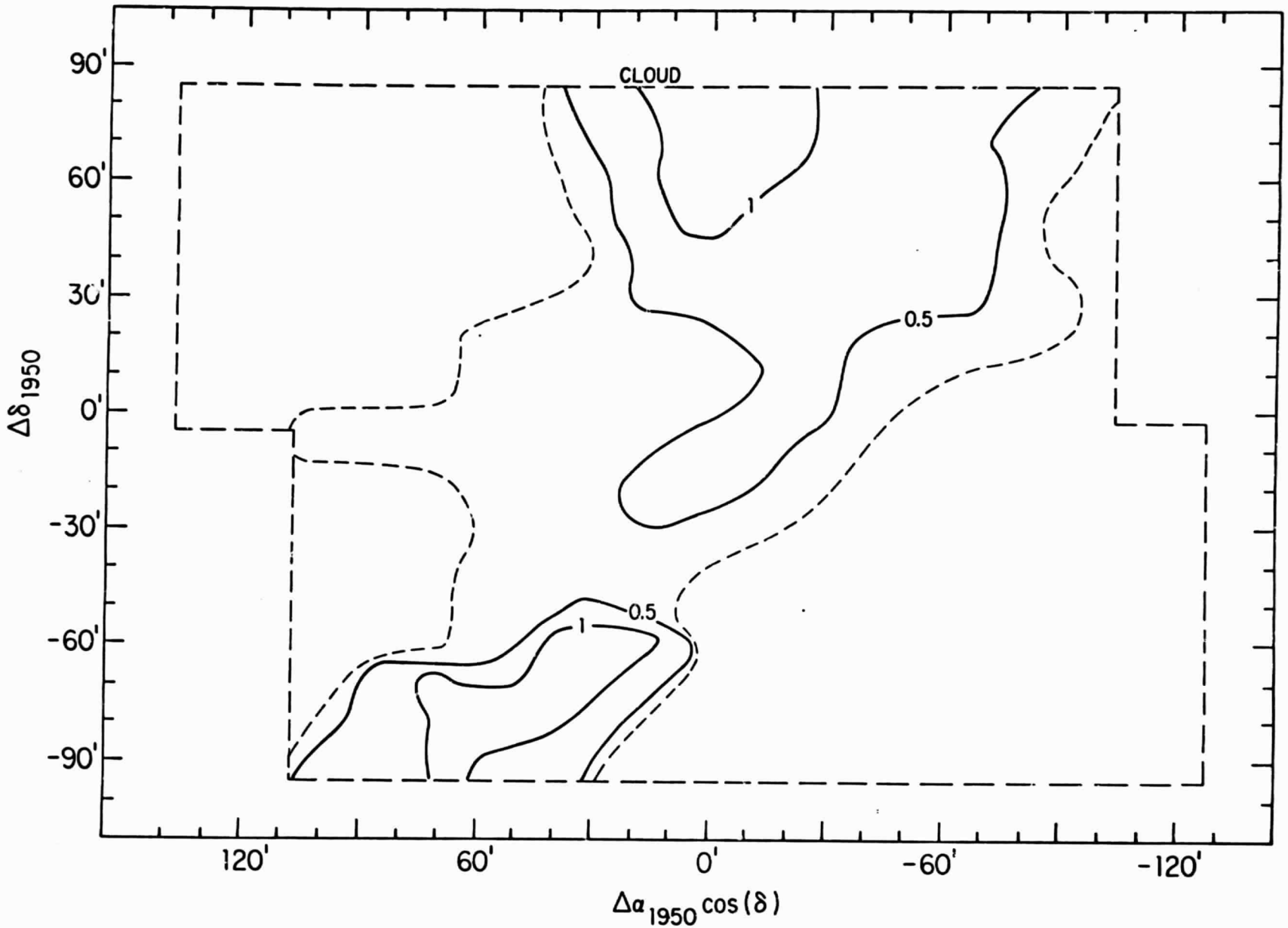
CLOUD
1
0.5
0.5
1
90'
60'
30'
0'
-30'
-60'
-90'
120'
60'
0'
-60'
-120'
$\Delta\delta_{1950}$
$\Delta\alpha_{1950}\cos(\delta)$

Fig 4c

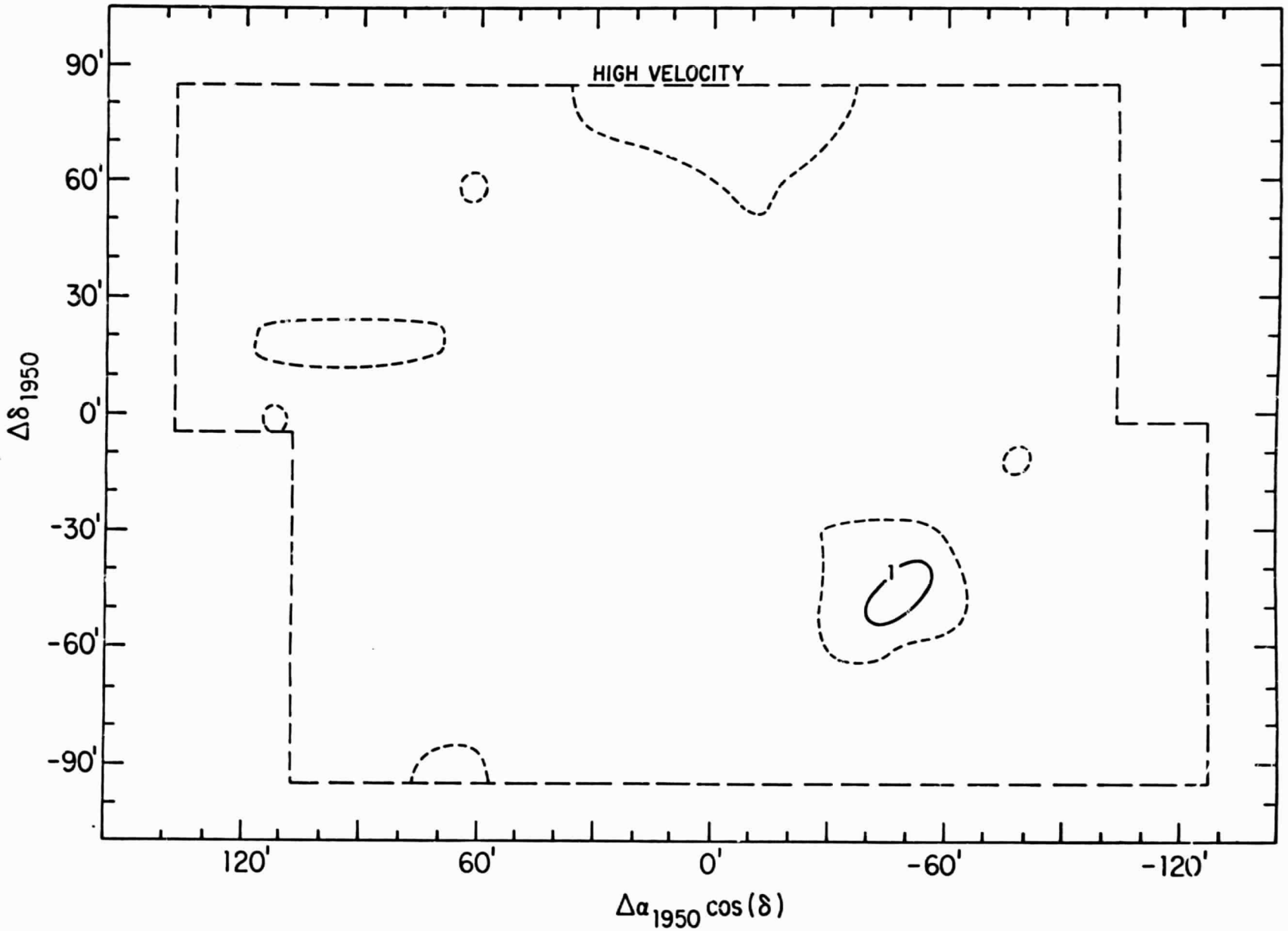
HIGH VELOCITY
90'
60'
30'
0'
-30'
-60'
-90'
$\Delta\delta_{1950}$
120'
60'
0'
-60'
-120'
$\Delta\alpha_{1950}\cos(\delta)$

Fig 4d

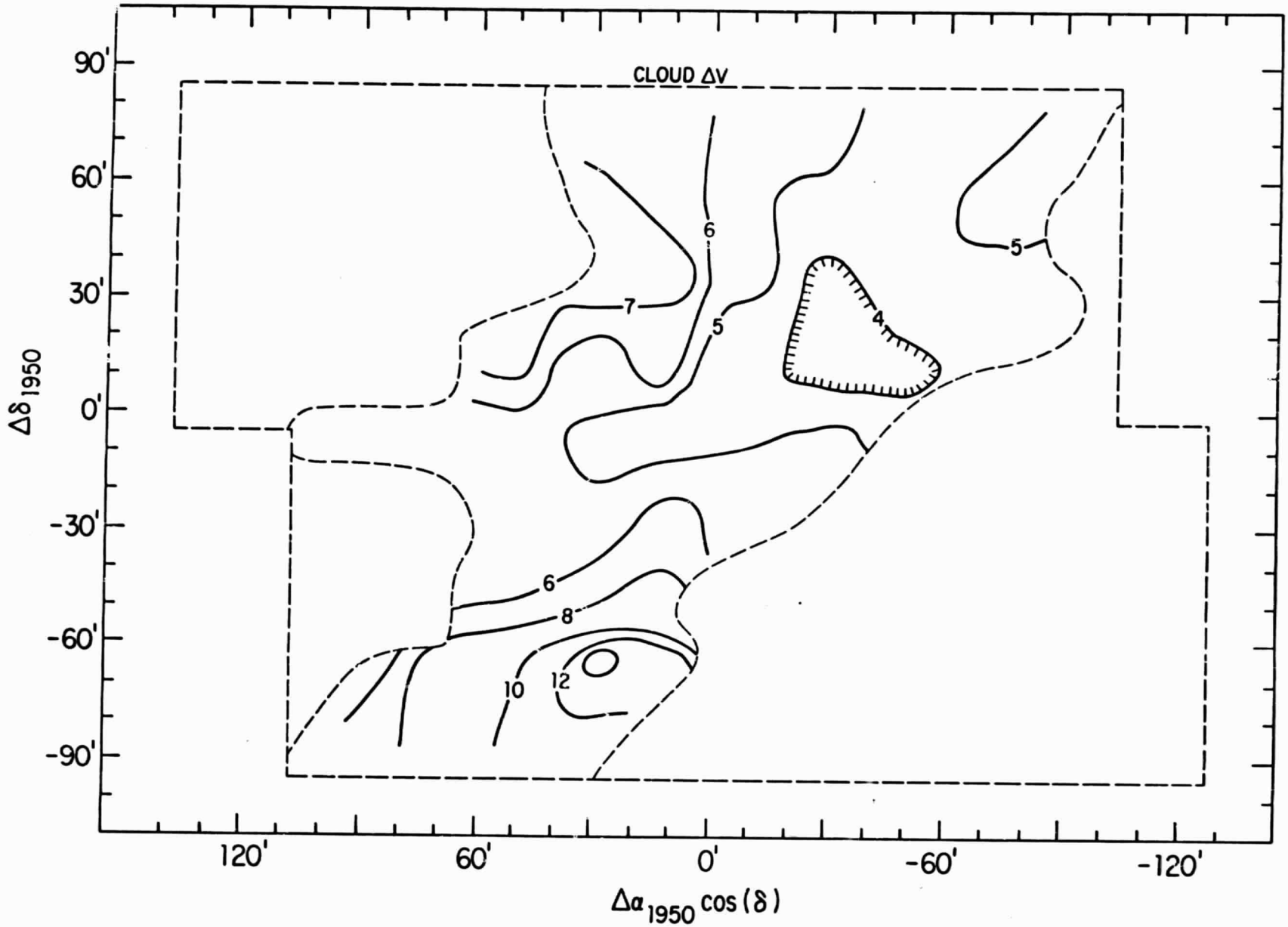
CLOUD ΔV
90'
60'
30'
0'
-30'
-60'
-90'
Δδ1950
120'
60'
0'
-60'
-120'
Δα1950 cos (δ)
7
6
5
4
5
6
8
10
12

Fig 5a

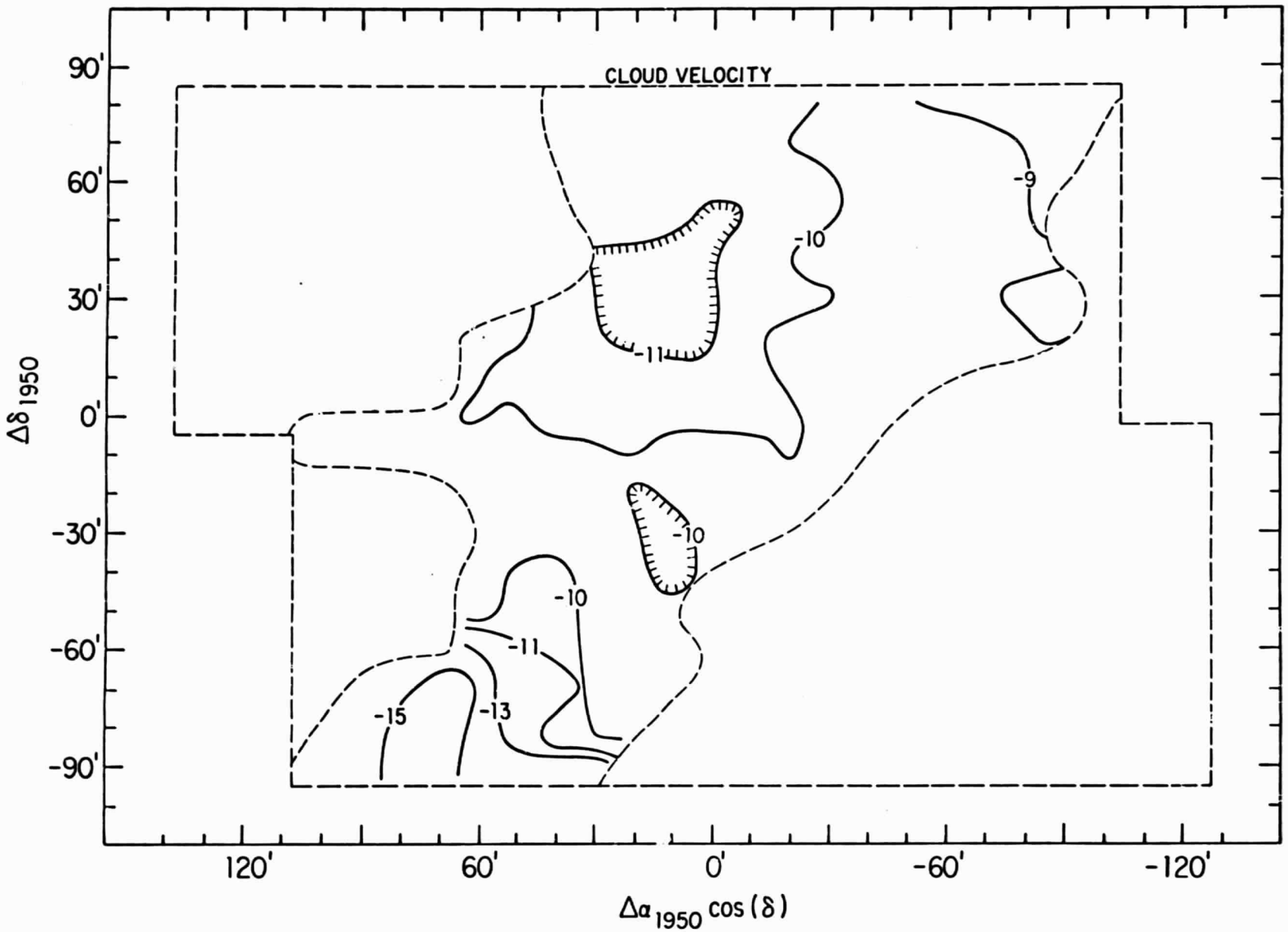
CLOUD VELOCITY
90'
60'
30'
0'
-30'
-60'
-90'
$\Delta\delta_{1950}$
120'
60'
0'
-60'
-120'
$\Delta\alpha_{1950}\cos(\delta)$
-9
-10
-11
-10
-10
-11
-15
-13

Fig 5b

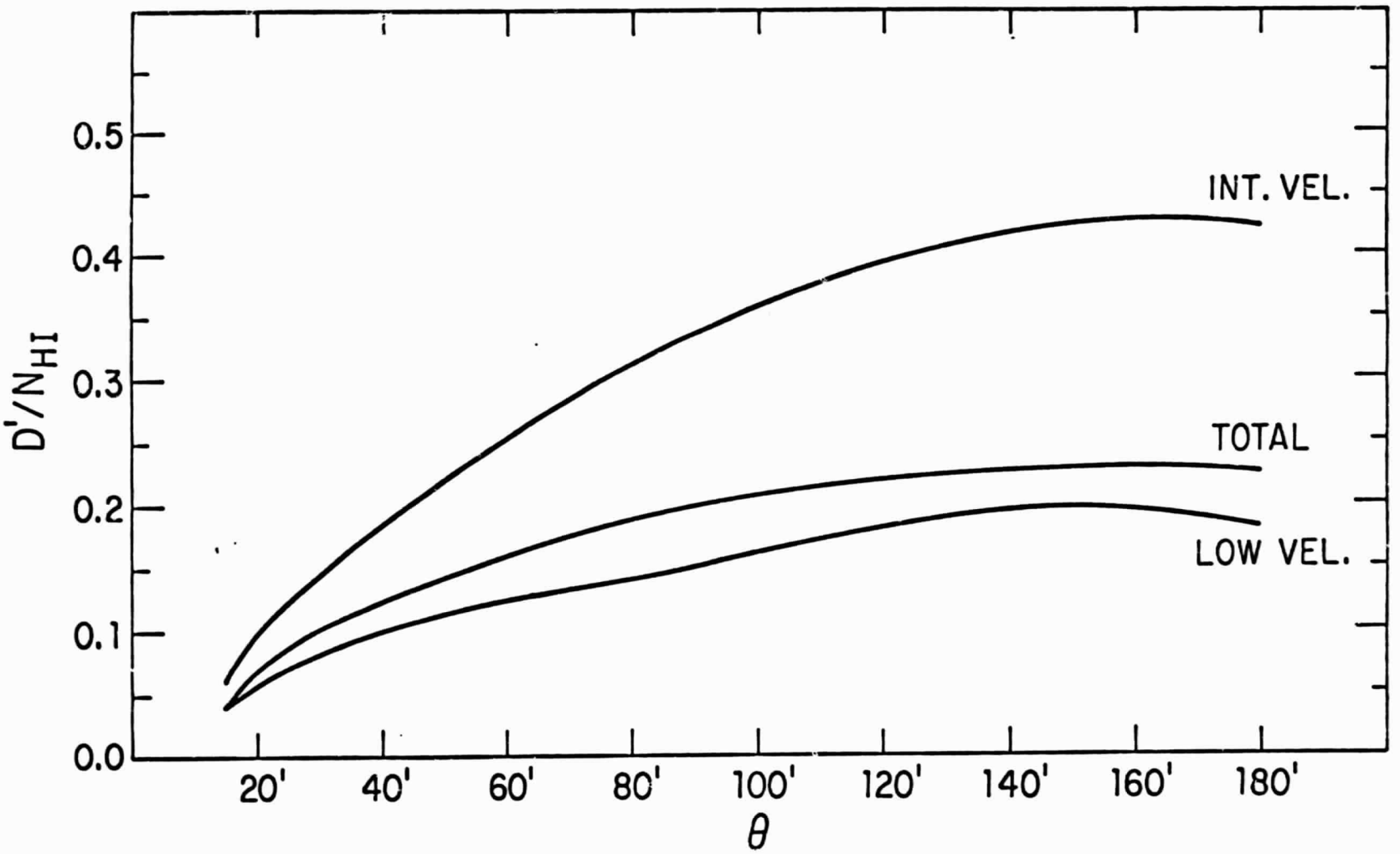
0.5
0.4
0.3
0.2
0.1
0.0
D'/N_HI
INT. VEL.
TOTAL
LOW VEL.
20'
40'
60'
80'
100'
120'
140'
160'
180'
θ

Fig 6

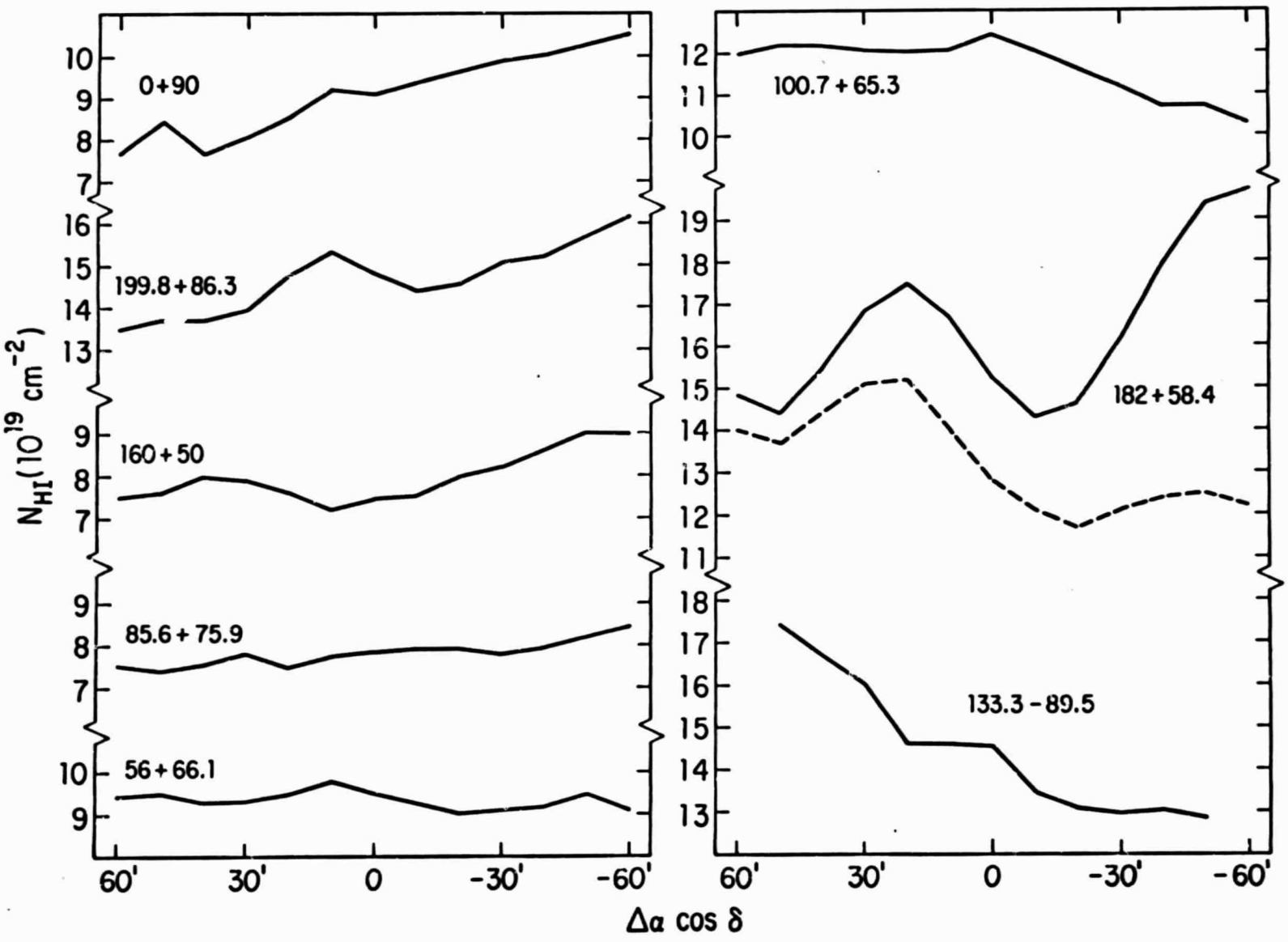
0+90
199.8+86.3
160+50
85.6+75.9
56+66.1
100.7+65.3
182+58.4
133.3-89.5
$N_{HI}(10^{19}\ cm^{-2})$
60'
30'
0
-30'
-60'
$\Delta\alpha \cos\delta$

Fig. 7

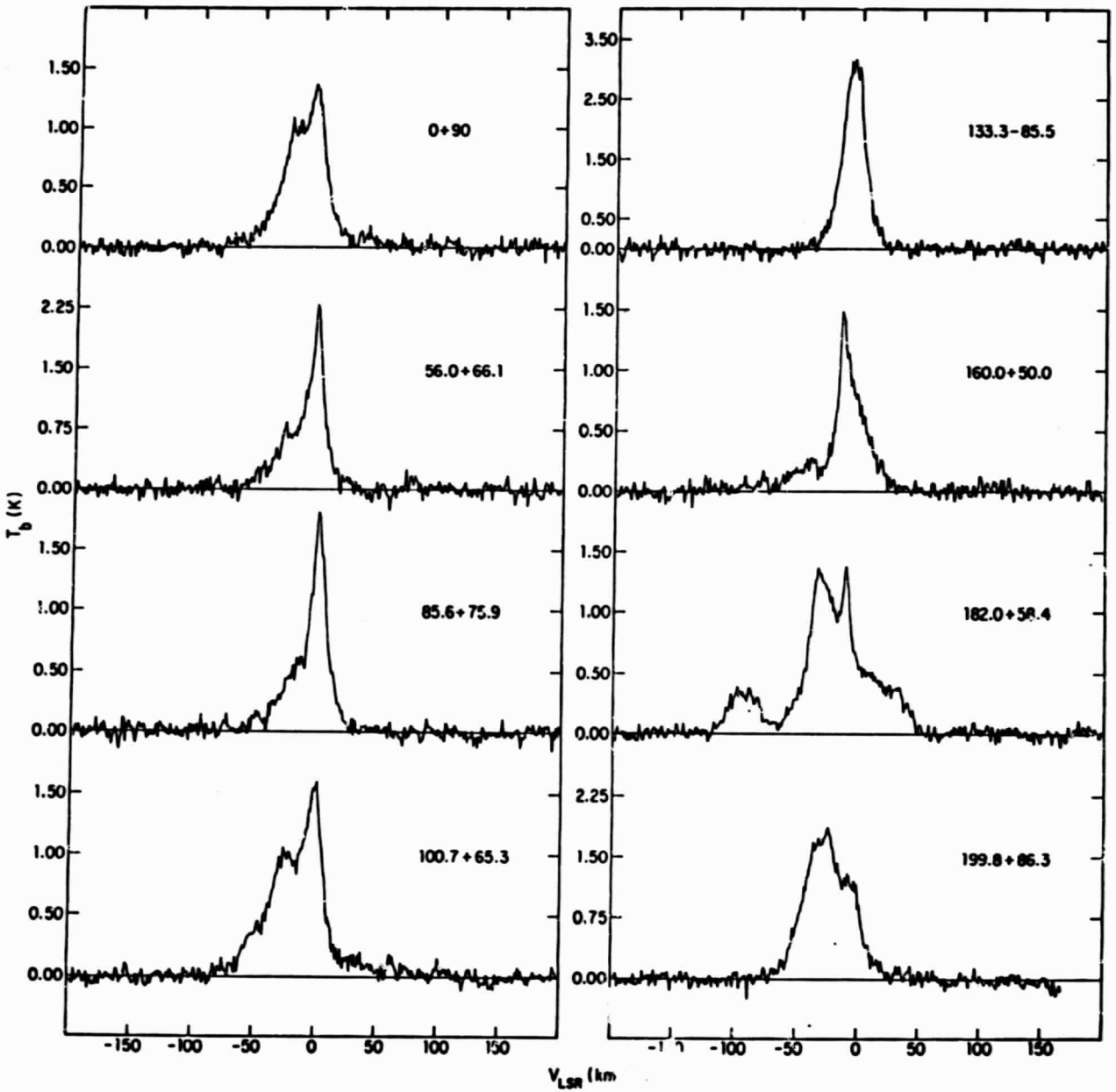
0+90
133.3-85.5
56.0+66.1
160.0+50.0
85.6+75.9
182.0+58.4
100.7+65.3
199.8+86.3
T_b (K)
V_LSR (km

Fig. 8

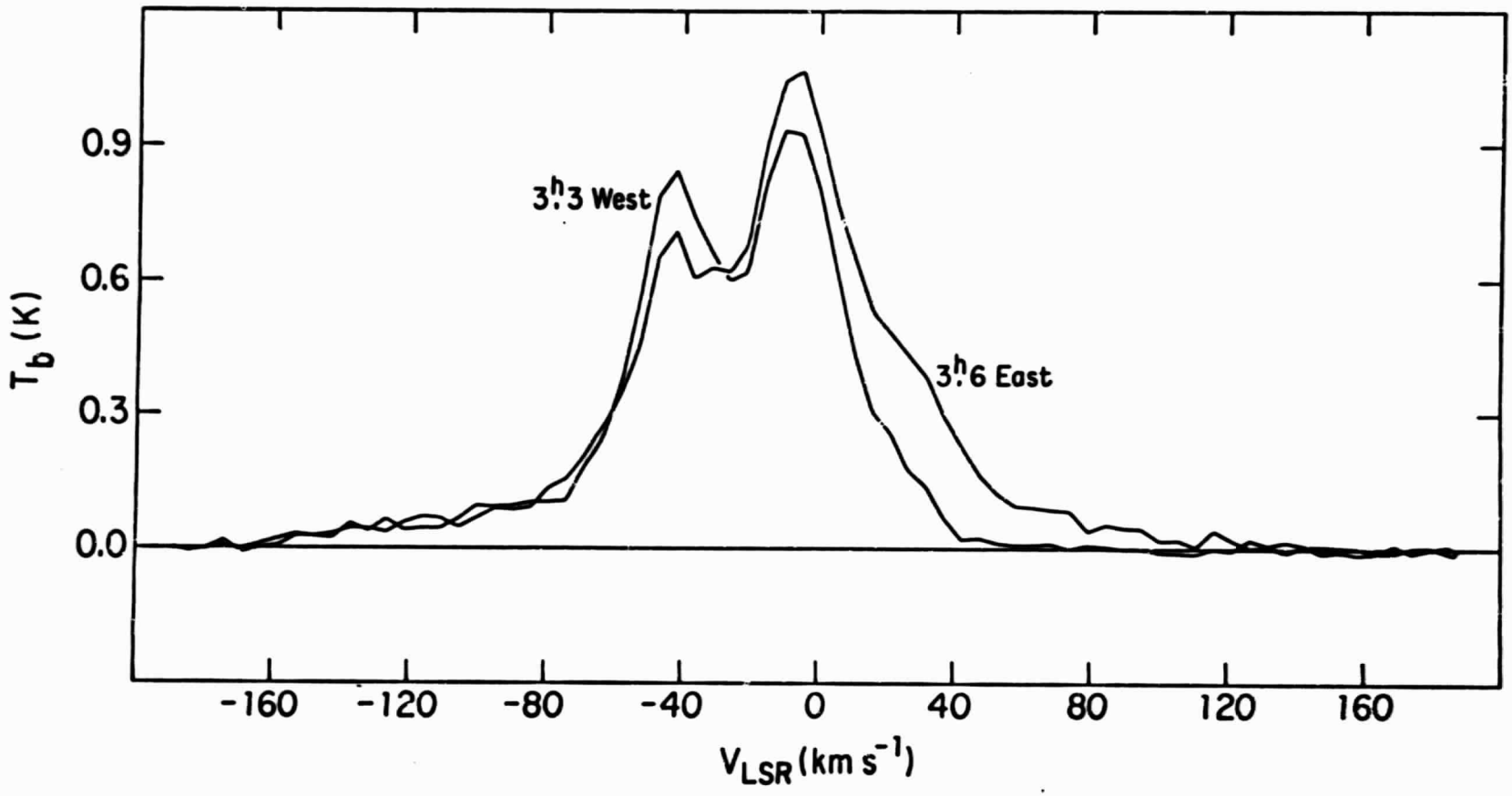
0.9
0.6
0.3
0.0
T_b (K)
$3^h.3$ West
$3^h.6$ East
-160
-120
-80
-40
0
40
80
120
160
V_{LSR} (km s^{-1})

Fig. 9

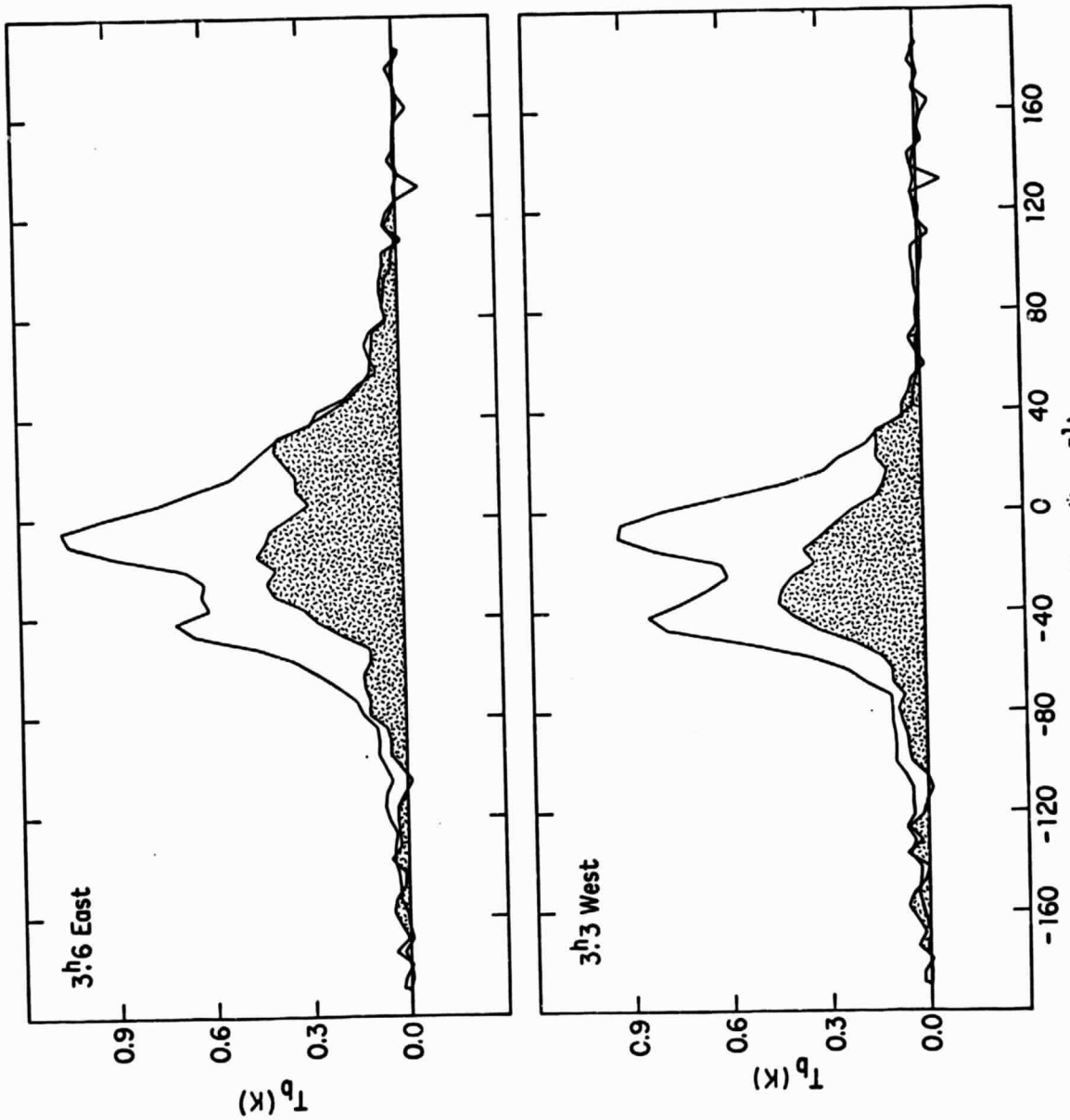

Fig. 10

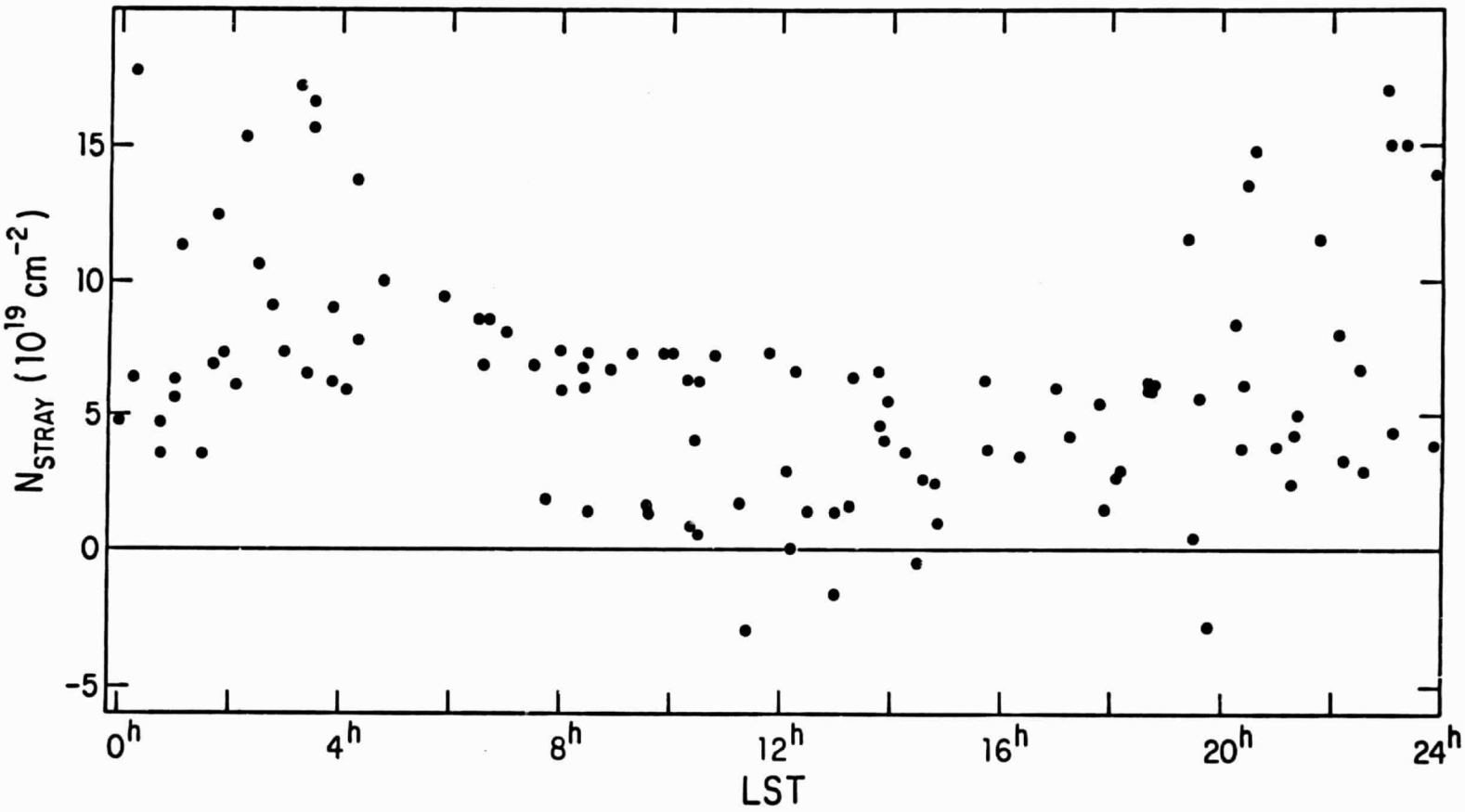

Fig. 11

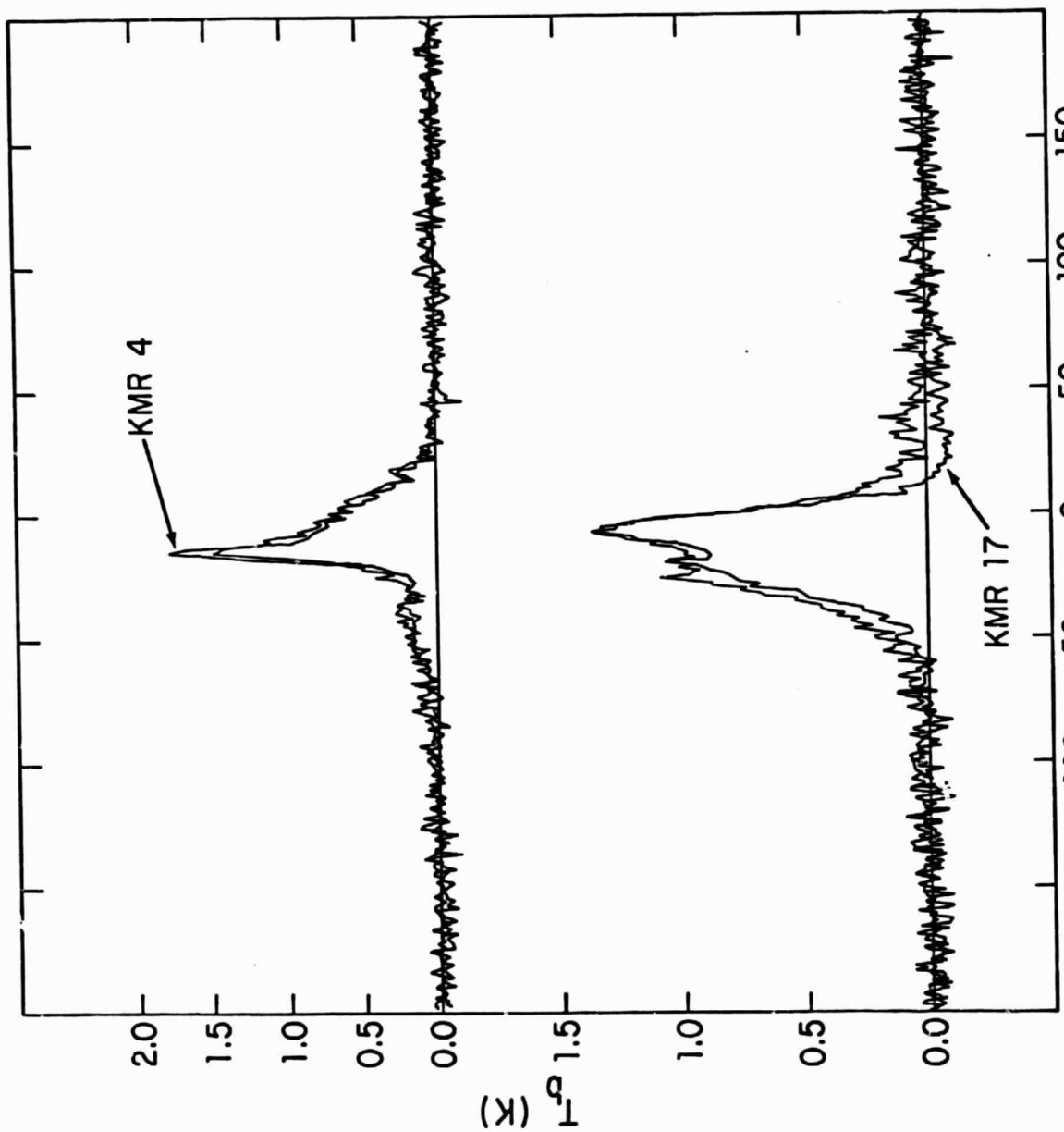

Fig. 12